Czech Technical University in Prague

Faculty of Electrical Engineering
Department of Cybernetics
Multi-robot Systems

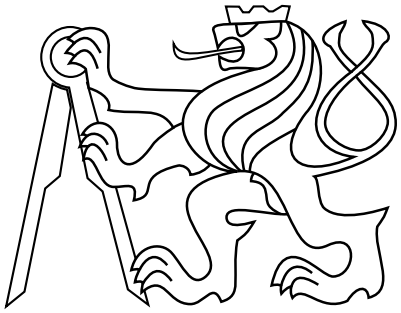

Adaptive Local Binarization to Improve the Performance of the UVDAR-COM System

Master's Thesis

Marlon Rivera Muñoz

Prague, May 2024

Study programme: Cybernetics and Robotics
Supervisor: Daniel Bonilla Licea, Ph.D.

Acknowledgments

I express my gratitude to my supervisor, Daniel Bonilla Licea, Ph.D., for his time, support, and guidance throughout the work for this thesis. M.Sc Tim Lakemann for his support with ideas and evaluation during the project. Ing. Viktor Walter for his support and expertise in evaluating the solutions presented and his ideas to improve the solution. I would also like to thank the MRS team for opening the doors to continuing learning and teachings during the experimental campaign. Without any of the mentioned, the development of this project would not have been possible. To my family, thank you is an understatement for the support you have given me throughout my life. Today I am far away from the people who love and appreciate me the most, and that supported me with the desire to come abroad to study what I am passionate about. Thank you for being a daily source of motivation to make the sacrifice of not being home worth it.

MASTER‘S THESIS ASSIGNMENT

I. Personal and study details

Student's name: **Rivera Marlon** Personal ID number: **516508**

Faculty / Institute: **Faculty of Electrical Engineering**

Department / Institute: **Department of Cybernetics**

Study program: **Cybernetics and Robotics**

II. Master’s thesis details

Master’s thesis title in English:

Adaptive Local Binarization to Improve the Performance of the UVDAR-COM System

Master’s thesis title in Czech:

Zlepšení kvality systému UVDAR-COMM pomocí adaptivního prahování

Guidelines:

The Ultraviolet Direction and Ranging (UVDAR) system is utilized for mutual relative localization and communication between multiple Unmanned Aerial Vehicles (UAVs), utilizing UV-LEDs attached to the UAVs for data transmission. The system employs calibrated grayscale cameras that are sensitive to UV light, which are equipped with UV bandpass filters and wide-angle lenses for data reception and decoding.
The UVDAR system employs static binarization to process captured images into a binary format, highlighting UV-LEDs as white spots against a reduced background, crucial for filtering out visible light and simplifying UV light extraction. Facilitating the subsequent identification, tracking, and decoding of UV-LED sequences for UAV localization and communication.
Guidelines:
1. Review the state of the art in Optical Camera Communications (OCC) within the context of Unmanned Aerial Vehicles (UAVs). [1] [2]. Discuss the challenges and differences of traditional OCC to make it work properly on UAV applications (compulsory).
2. Review the state of the Ultraviolet Direction and Ranging (UVDAR) system used for mutual relative localization and communication between UAVs . [3][4][5]. Discuss the open problems not solved by the current binarization algorithm (compulsory).
3. Perform a comprehensive analysis of the experimental data collected from the UVDAR system to determine the limitations of the static binarization and characterize the noise of the UVDAR system (compulsory).
4. Design and implement a method for adaptive binarization suitable for real-time processing, take inspiration from current methods such as [2] (compulsory).
5. Evaluate the performance of the adaptive binarization algorithm and compare it with the current static binarization method in the UVDAR system. [3] (compulsory).
6. Design and execute experiments to validate the performance of the proposed method, evaluating the system communication capabilities: communication range, bit error rate and data rate (optional).

Bibliography / sources:

[1] Nam Tuan Le, Mohammad Arif Hossain, Yeong Min Jang, A survey of design and implementation for optical camera communication, Signal Processing: Image Communication, Volume 53, 2017.
[2] H. Takano, M. Nakahara, K. Suzuoki, Y. Nakayama and D. Hisano, "300-Meter Long-Range Optical Camera Communication on RGB-LED-Equipped Drone and Object-Detecting Camera," in IEEE Access, vol. 10, pp. 55073-55080, 2022, doi: 10.1109/ACCESS.2022.3177140.
[3] Jiri Horyna, Viktor Walter and Martin Saska. UVDAR-COM: UV-Based Relative Localization of UAVs with Integrated Optical Communication. In 2022 International Conference on Unmanned Aircraft Systems (ICUAS). June 2022
[4] V Walter, M Saska and A Franchi. Fast mutual relative localization of uavs using ultraviolet led markers. In 2018 International Conference on Unmanned Aircraft System (ICUAS 2018). 2018
[5] V Walter, N Staub, A Franchi and M Saska. UVDAR System for Visual Relative Localization With Application to Leader–Follower Formations of Multirotor UAVs. IEEE Robotics and Automation Letters 4(3):2637-2644, July 2019.

Name and workplace of master's thesis supervisor:

Daniel Bonilla Licea, Ph.D. Multi-robot Systems FEE

Name and workplace of second master's thesis supervisor or consultant:

Date of master's thesis assignment: **14.02.2024** Deadline for master's thesis submission: **24.05.2024**

Assignment valid until: **21.09.2025**

Daniel Bonilla Licea, Ph.D.	prof. Dr. Ing. Jan Kybic	prof. Mgr. Petr Páta, Ph.D.
Supervisor's signature	Head of department's signature	Dean's signature

III. Assignment receipt

The student acknowledges that the master's thesis is an individual work. The student must produce his thesis without the assistance of others, with the exception of provided consultations. Within the master's thesis, the author must state the names of consultants and include a list of references.

. Date of assignment receipt

Student's signature

Declaration

I declare that presented work was developed independently, and that I have listed all sources of information used within, in accordance with the Methodical instructions for observing ethical principles in preparation of university theses.

Prague, 24.05.2024 Marlon Rivera Muñoz

Abstract

The development, application, and assessment of an adaptive thresholding algorithm are the main subjects of this thesis. Based on the Ultraviolet Direction and Ranging (UVDAR), a system for mutual-relative localization and communication between multi-Unmanned Aerial Vehicle (UAV) systems. The main focus of the algorithm design is to propose a solution to the limitations of the current system with different distances and orientations due to the state-of-the-art detection method using static thresholding. The adaptive algorithm uses Region of Interest (ROI)s built based on information received from the tracking algorithm as feedback, performing local processing of multiple signals by adjusting to the intensity of each. The system is verified in simulation and real-world experiments, demonstrating the performance improvement with the proposed method.

Keywords UVDAR, Unmanned Aerial Vehicles, Adaptive Thresholding Algorithm, UV-LED detection, Regions of Interest, Communication Performance

Abstrakt

Vývoj, aplikace a hodnocení adaptivního algoritmu prahování jsou hlavními tématy této práce. Na základě systému UVDAR, systému pro vzájemnou relativní lokalizaci a komunikaci mezi systémy s více bezpilotními letadly. Hlavním zaměřením návrhu algoritmu je navrhnout řešení omezení současného systému s různými vzdálenostmi a orientacemi v důsledku nejmodernější metody využívající statické prahování. Adaptivní algoritmus používá ROI sestavené na základě informací získaných od sledovacího algoritmu jako zpětnou vazbu a provádí lokální zpracování více signálů přizpůsobením intenzity každého z nich. Systém je ověřen v simulačních a reálných experimentech, které prokazují zlepšení výkonu pomocí navržené metody.

Klíčová slova UVDAR, bezpilotní letadla, algoritmus adaptivního prahování, detekce UV-LED, oblasti zájmu, výkonnost komunikace

Abbreviations

4DHT 4D Hough Transform

AMI Anonymous Blinking Marker trackIng

BER Bit-Error-Rate

CCA Connected Component Analysis

CDF Cumulative Distribution Function:

CDF Cumulative Distribution Function

CNN Convolutional Neural Network

CPx Communication Pixel Array

CTU Czech Technical University

FAST Features from Accelerated Segment Test

FOV Field-of-View

GNSS Global Navigation Satellite System

KF Kalman Filter

KL Kullback-Leibler

LED Light Emitting Diode

LoS Line of Sight

MIMO Multiple-Input-Multiple-Output

MRS Multi-Robot-Systems

NLoS Non-Line of Sight

NRZ Non-Return-to-Zero

OCI Communication Image Sensor

OCC Optical Camera Communication

OOK On-Off Keying

OWC Optical Wireless Communication

PDF Probability Density Function

PMF Probability Mass Function

Px Image Pixel Array

RF Radio Frequency

ROI Region of Interest

RTK Real-time Kinematics

RTK Real-Time Kinematic

RX Receiver

SNR Signal-to-Noise ratio

SOTA State-of-the-art

TX Transmitter

UAV Unmanned Aerial Vehicle

UFSOOK Under Sampled Frequency Shift On-Off Keying

UPSOOK Undersampled Phase Shift ON-OFF Keying

UT Unscented Transform

UV Ultra Violet

UVDAR Ultraviolet Direction and Ranging

V2V Vehicle-to-Vehicle

VLC Visible Light Communication

YOLO You Only Look Once

Contents

List of Figures

List of Tables

0 List of Algorithms

1 Introduction

Contents

In recent years, Optical Camera Communication (OCC) communication systems development has emerged as an alternative to existing Radio Frequency (RF) communications, as RF demand for communication services continues to grow [34], and satisfying it will be increasingly challenging with the growth of smart devices. The utilization of the light spectrum by systems for smart device communication, localization, and navigation introduces an underutilized spectrum to be used.

The adoption of UAVs for communication applications is expected to improve coverage and spectral efficiency as compared to traditional ground-based stations [29]. In particular, OCC use in mobile systems such as UAVs and robotic platforms presents a new opportunity for solutions to existing robotic problems. The interaction and collaboration between robotic systems demand a robust and accurate system for localization and communication between its members, something that in real-world applications can become challenging. This is because, it is necessary to confront environments where effective communication is not available or degraded due to environmental conditions, a lack of infrastructure, or interference that complicates localization and navigation tasks.

Therefore, the dependence on traditional systems has motivated the search for alternatives to provide a solution to such scenarios, and interest in relative localization systems has grown in recent years. OCC provides an alternative that complements the search for systems independent of RF infrastructure and facilitates relative localization by integrating Light Emitting Diode (LED)s into multi-robot systems used jointly for communication and localization.

This motivation led to the development of the UVDAR system by the Multi-Robot-Systems (MRS) group at the Department of Cybernetics from Czech Technical University (CTU), using Ultra Violet (UV) LEDs to facilitate detection among multi-UAV systems to achieve its localization, equipped with the ability to transmit information with the decoding of optical signals transmitted from the UV LEDs. Both the OCC and the UVDAR system are discussed in more detail in chapter 2.

1.1 Objective

This work aims to analyze the current UVDAR system, discussing the potential limitations of the reception of optical signals. The objective is to optimize the reception to increase decoding accuracy and communication range. Currently, the LED detection algorithm uses a pre-defined intensity threshold, which presents a potential bottleneck due to the intensity variations of the LEDs given signal attenuation. Having receivers capturing a range of intensities, in scenarios with combination of diverse UAVs positioned at various distances and orientations, together with optical properties that vary in reception angles and distances. Problems this thesis aims to solve with an adaptive thresholding algorithm.

1.2 Related work

To our knowledge, no published work would take a similar approach for the adaptive detection of LEDs with UAV OCC. Recent work in the field has presented machine learning approaches, specifically deep learning methods for the task of the LED detections equipped in UAVs for communication [13]. The methods of SVM and Convolutional Neural Network (CNN) for classification and decoding are employed to develop an intelligent optical receiver [23].

However, early approaches in the area of Visible Light Communication (VLC) literature exist using the adaptive approach and evaluating performance with static thresholding schemes. The authors in [22] demonstrate a significant difference in performance with adaptive techniques about operating distance and Bit-Error-Rate (BER). The paper [33] uses adaptive techniques, not only for thresholding in the detection but also in the demodulation of the patterns received from the LED, achieving orders of magnitude improvement in BER compared to static thresholding methods.

An adaptive thresholding system is proposed in [19], achieving improved BER under varying illumination conditions, where the authors use a threshold calculated based on a first-order differential equation, calculating the adaptive threshold between consecutive times. However, the calculation depends on the previous threshold used, which would increase the complexity of having multiple TXs. For our application, having a single prior threshold is insufficient, as the UVDAR is intended for multi-robot operation, having various TXs with different distances, orientations and intensity values. As a result, to maintain a previous threshold value, it would be required to give each TX a distinct prior threshold, introducing complexity requiring not only detection but also assignment problems.

Finally, different techniques have been presented in the area of detection and tracking, such as optical flow for the detection of UAVs [32] or techniques for the identification of moving objects, demonstrating the advantage of complementing detection with tracking for UAV applications [42].

1.3 Contributions

This thesis presents an thresholding algorithm designed for operation in the UVDAR system. The main objective is the implementation of adaptive thresholding algorithm to overcome the limitations of attenuation and intensity variation in LEDs. Employing an ROI approach to improve accuracy by evaluating local signal conditions, The ROIs are constructed based on the information provided by the tracking algorithm from the system and used as feedback for the integration of the adaptive processing in the current architecture. Due to the local processing of each point, it's possible to process different signals simultaneously in parallel, adapting to each individual light source. Essential for multi-robot operations that have multiple receivers with various different distances and intensity values. The design of the adaptive algorithm aims to fulfill this function achieving real-time operation, the algorithm was evaluated in simulations and real-world experiments.

2 Preliminaries

Contents

2.1 Optical Camera Communications (OCC)

Among the several types of Optical Wireless Communication (OWC) technologies, we have Optical Camera Communication (OCC) that distinguishes itself from traditional optical communications, such as VLC systems, by the utilization of a camera as receiver instead of a photo-diode [39].

The fundamental principle of OCC involves the modulation of light sources, commonly LEDs, for transmitting encoded information. The information is then captured and decoded by a camera. The procedure involves adjusting the intensity, color, or spatio-temporal pattern of light, which is then captured by the camera and then processed with image processing algorithms [45]. Modulation can range from basic On-Off Keying (OOK), which involves turning a light source on and off, to more sophisticated methods that use color and spatial modulation to enhance data transmission speeds [7]. One advantage of OCC is its capacity to seamlessly operate as a Multiple-Input-Multiple-Output (MIMO) system, having multiple LEDs in the camera image and decoding several bits in a single instance,despite coming from different sources.

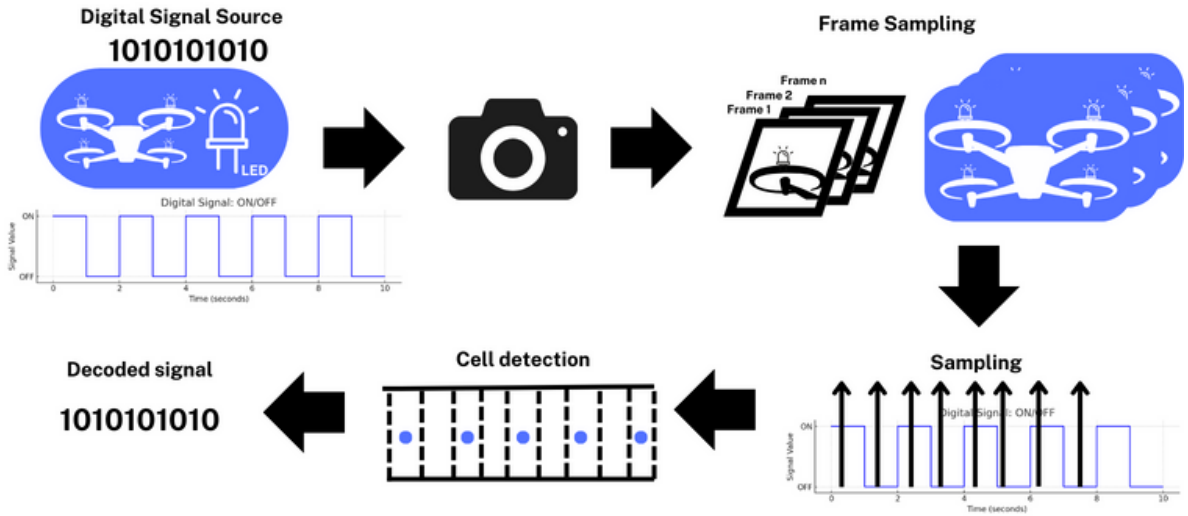

Figure 2.1: OCC architecture concept.

OCC has great potential for modern communication systems, mainly because of its high Signal-to-Noise ratio (SNR) [35] and built-in security properties. Unlike other wireless communication techniques that utilizes radio frequencies, this particular approach reduces

the potential of interference with other devices and decreases security risks due to its line-of-sight characteristic [6]. Because OCC relies on a direct Line of Sight (LoS) between Receiver (RX) and TX; jamming, intercepting, or eavesdropping attacks become significantly more complicated to achieve. Attackers in RF systems can disrupt the signal at a distance, but in OCC, it would be necessary to be in the field of view to achieve the attack, making it easier to detect and act to avoid such attacks. [25] In environments where conventional RF communications may be impractical or prohibited, OCC systems present new opportunities for the secure transmission of data, situations as in remote or rural areas with underdeveloped or non-existent infrastructure with no internet or cellular coverage, or in facilities where RF devices present a risk given interference with sensitive devices.

- **Performance Effects**

Image Sensor Architecture

The performance of OCC is significantly dependent on the camera architecture and characteristics. The attributes of the camera sensors, such as their shutter modes (global and rolling), considerably impact the performance of OCC systems. The rolling shutter mode causes difficulties due to its row-by-row collection of pixels, with pixel lines of the image created at different times, which might result in motion blur [39]. However, it also allows recording multiple states of the light source capturing more information [26]. In contrast, the global shutter mode records all pixels in a single instance, reducing motion blur and improving image clarity for objects in motion. However, the data rate is reduced by recording a single state for each image.

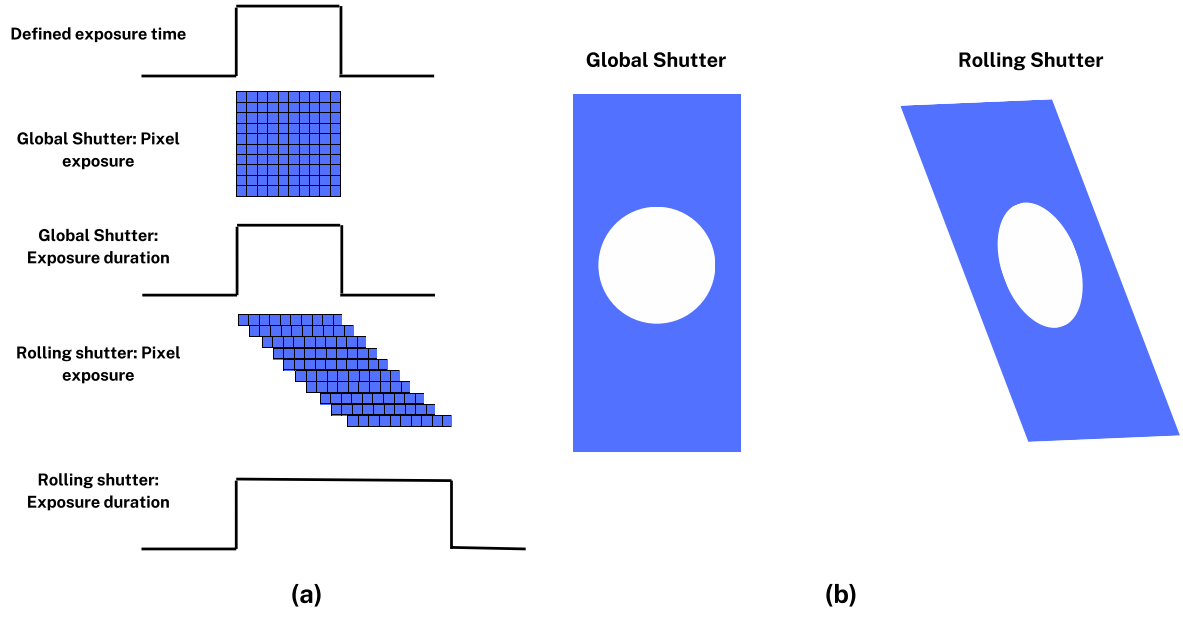

Figure 2.2: (a) Image construction comparison (b) Rolling shutter effect.

Data Rate

The image sensor designs we previously discussed primarily determine the data rate performance of OCC systems. When using the rolling shutter mode, it is necessary to consider factors such as image skew and camera resolution [39]. In addition, the LED's frequency response needs to be lower than the camera frame rate to avoid information loss, and if the source is slower bits are duplicated. Even if the nominal bit duration and nominal sample period of the camera are the same, there will still be discrepancies given the imperfections of clock signals from TX and RX [4]. Alternatively, the global shutter mode relies on the camera frame rate, decoding each bit for each source. Under the constraint that the bit duration needs to be longer than the camera's exposure time to prevent recording both the ON and OFF states of the LED.

Perspective Distortion

Perspective distortion, the visual deformation of the image size or shape results in a decrease in the light intensity received at the camera pixel, depending on the lens focus and camera angle. An ideal situation occurs when the light from the transmitter targets directly on the camera, therefore ensuring effective light absorption while minimizing energy loss. On the contrary, perspective distortion results in pixel intensity that is both distorted and out of focus due to obstructions caused by the aperture of the camera [36], affecting the performance of the system [44], this effect termed as well as inter-pixel interference, degrading signal quality and information capacity. [21]

2.2 State of the Art

Given that camera-equipped devices have grown increasingly popular, OCC is emerging as a significant technology for OWC, enabling data transmission through the transmission of visible light. Most recent advances have focused on increasing data transmission rates, robustness under various lighting conditions, and expanding the scope of applications. Established as a significant area of study given its accomplishments of high rates, advanced modulation techniques, and integration with mobile technology [20],[27].

The development of scalable and efficient OCC systems has been made possible with the integration of advances in image processing, sensor technology, and mobile devices demonstrating the viability of OCC for real-world situations. Modulation and coding schemes specifically suited to the special properties of camera sensors are one of the significant developments in OCC. Under Sampled Frequency Shift On-Off Keying (UFSOOK) and Undersampled Phase Shift ON-OFF Keying (UPSOOK) together has been researched for reliable and effective high-rate data transmission [30].

Technical Advancements and Applications

To enhance Vehicle-to-Vehicle (V2V)communication, the authors [46] created a system utilizing LED transmitters and a camera receiver paired with a Communication Image Sensor (OCI), focusing on achieving reliable and rapid data transfer in variable lighting conditions. The significant improvements to the OCI are the Communication Pixel Array (CPx), which lets light optical signals respond quickly, and the "1-bit flag" Image Pixel Array (Px) method, which tells the difference between high-intensity LEDs and backgrounds to accurately track in real-time reducing the occurrence of incorrect detections improving signal reception.

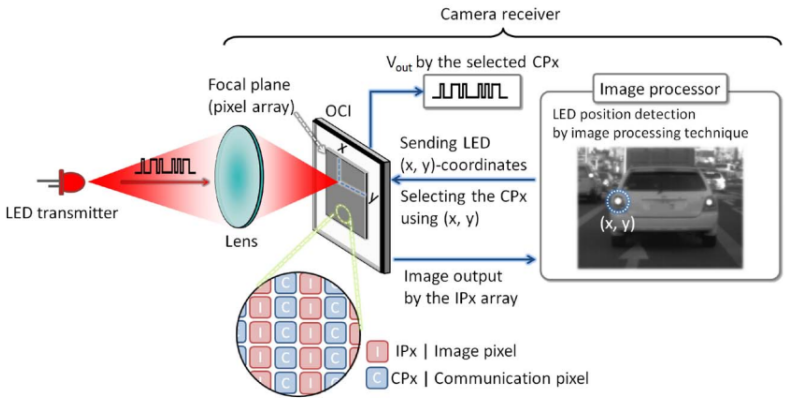

Figure 2.3: Basic operations of IS-OWC system Fig. 3 in [46].

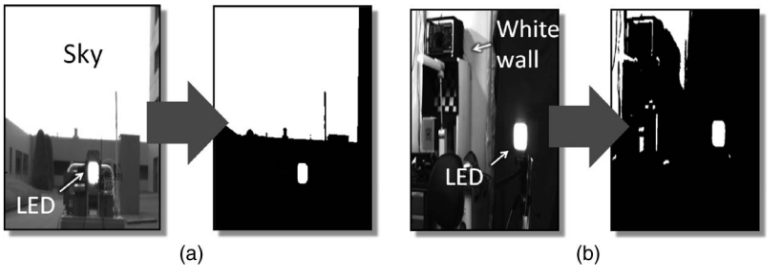

Figure 2.4: LED detection using gray images Fig. 6 in [46].

Authors of [41] demonstrated an RGB LED-based OCC system operating over long distances with high spectral efficiency. The data transmission rate of 150 bits per second across a distance of 60 meters was achieved by using a single RGB LED together with a DSLR camera integrated with an OCI for the LED detection, as shown in [46], demonstrating the importance that accurate image processing methods to improve the system's ability to detect LED signals across various ranges, improving the potential of long-range, non-flickering VLC communication system.

Relevant results on the performance of an RGB LED-based OCC system at different distances are demonstrated in [43]. The study displayed how with increasing distance the LED intensity is reduced. The decrease reaches a stable state beyond 60 meters as a result of the combined effect of gamma correction and the inverse square law, which affects the intensity of light. At the same time, the BER measurement stays constant at 150 bits per second across a distance of 25 meters, with minimal BER. However, when the distance grows, especially up to 60 meters, the BER experiences a significant increase

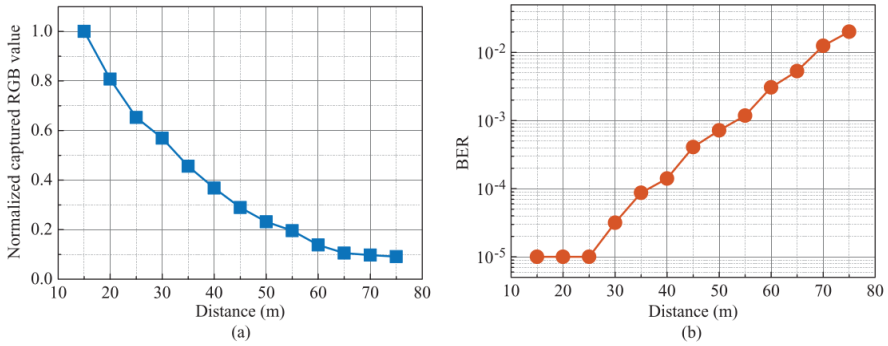

Figure 2.5: (a) Relative sum of captured RGB values, (b) BER performance on increasing distance Figure. 12 in [43].

In [40], IR-LED technology and OCC are used to improve indoor VLC. Uplink improvements achieved by applying a multi-frame decoding algorithm. By adjusting the frequency of the IR-LED and utilizing a two-dimensional Gaussian distribution fitting to analyze the light pattern, this method provides lower bit error rates and less saturation, resulting in enhanced data accuracy.

Additionally, the study findings demonstrate the intensity of IR-LEDs on images grows linearly with a current of up to 30 mA before reaching a saturation point. Experiencing a significant decrease when the distance between the camera increases from 0.5 to 1.5 m, experiencing a slight decrease beyond 1.5 m, with the intensity of LED increasing proportionally with longer exposure times on a logarithmic scale.

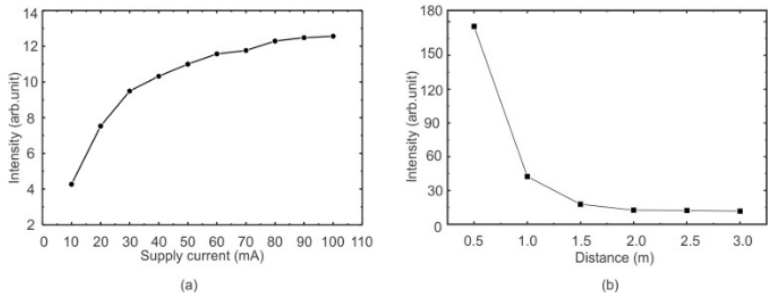

Figure 2.6: Intensity characteristics in conjunction with (a) supply current of LED and (b) communication distance Figure .4 in [40].

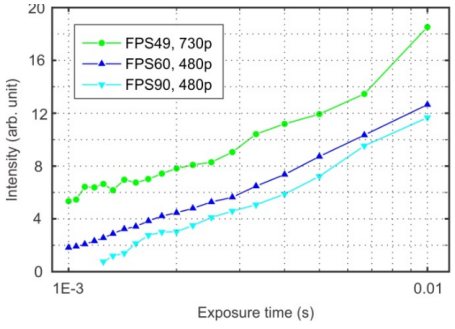

Figure 2.7: The variation of intensity of IR-LED on different exposure times Figure.5 in [40].

OCCs in UAVs and mobile platforms

OCC's versatility has resulted in its use in a wide range of applications, including UAVs and mobile platforms. The relevant systems that make use of OCC systems for localization or communication are introduced in this section.

Authors in [24], [14], [12] have shown that UAVs, equipped with RGB-LEDs and high-speed cameras, can achieve stable long-range communication for disaster recovery. This setup uses a CNN for precise LED detection utilizing the You Only Look Once (YOLO)v3 algorithm for quick ROI identification. The model was trained with a dataset of 2,000 images featuring the UAV equipped with the RGB-LEDs, combined with signal processing techniques to mitigate RGB signal interference. The approach enabled reliable communication over distances up to 300 meters, while reducing error rates. These results show the potential of OCC systems to enhance UAV capabilities. However, the study also highlights the need for advancements in image segmentation techniques to further improve this technology.

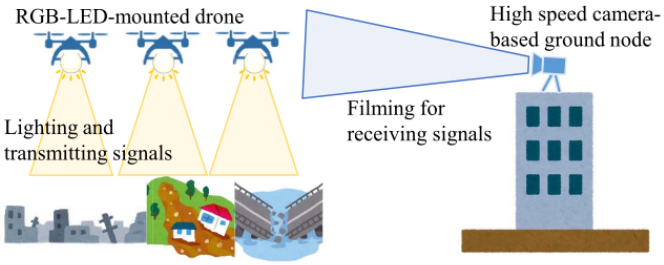

Figure 2.8: OCC system for disaster recovery. Figure. 1 in [14]

Authors from [2] attempted to improve UAV communications through a new approach for large Field-of-View (FOV) OWC. With the goal of increasing UAV networks' adaptability and bandwidth, The approach utilized an experimental configuration with a UAV equipped with an Light-Diffusing-Fiber Transmitter (LDF-Tx) and Long Short-Term Memory Neural Network (LSTMNN) for precise rolling-shutter-pattern decoding during UAV movements.

In [10], authors investigate the possibilities of UV communication and its application with the integration of OCC with UAVs to solve some of the most significant challenges of UAV swarm communications, like interference, a lack of radio frequency spectrum, and connectivity issues. Comparing visible light, mmWave, RF, and UV communication methods, mmWave's data rate was gigabits per second, with RF and visible light achieving megabits per second and UV Non-Line of Sight (NLoS) at kilobits per second. In contrast to the distance that RF can traverse several kilometers, the wavelengths of visible light, ultraviolet, and mmWave fall within the range of hundreds of meters. This comparison attempts to demonstrate that UV is a viable option for UAV swarm communication situations, even though having a lower data rate, it can support both LoS and NLoS communications without the interference problems of operating in the RF spectrum.

2.3 The UVDAR System

The MRS Group at Department of Cybernetics of the CTU in Prague, developed the UVDAR, a technology designed for mutual relative localization and communication among multiple UAVs [38]. Using calibrated grayscale cameras sensitive to UV light, equipped with wide-angle lenses and UV band-pass filters, the system uses UV LEDs mounted on the platforms to achieve fast mutual localization. Enhanced further to transmit and receive data from blinking sequences emitted by the UV LEDs; this function, known as UVDAR-COM, combines the UVDAR as an OCC system [11].

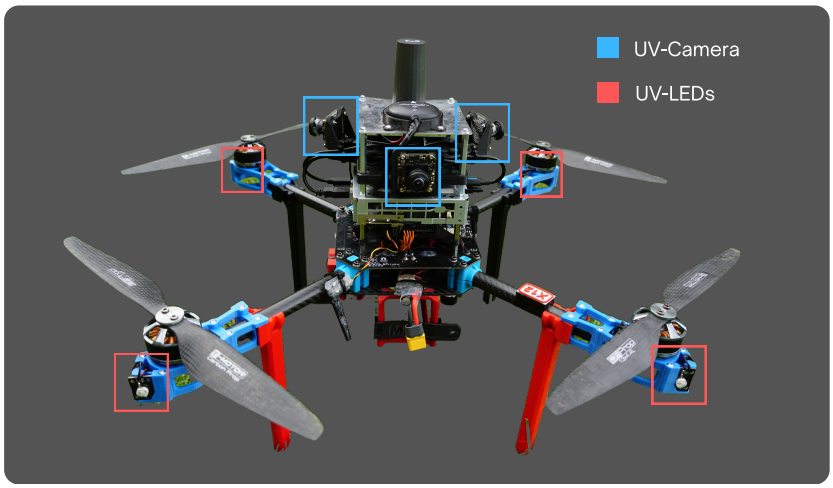

Figure 2.9: Front view of UAV platform with UVDAR components.

System Overview

As described in [38], UV light was chosen as the main source due to the requirement for a localization system that operates independently of illumination conditions. Since few sources of ultraviolet radiation exist in the the environment, mainly released by natural light sources like the sun, presents clear advantages for localization. In addition, the use of UV light lowers computational demand, as together with optical filters that remove the non-UV light and the background, makes the processing lighter in contrast of methods that operate in the visible spectrum. The approach is inspired by findings like the ones demonstrated in Fig. 2.10, where UV light makes it possible to clearly identify markers that are otherwise difficult to distinguish in the visible spectrum, even for modern CNN algorithms and the human eye.

Figure 2.10: Comparison with CNN, in a long-range and challenging background, UVDAR effectively identifies three UV markers as distinct brightness peaks Figure. 3 in [38].

The system has been used mainly in swarming applications; different authors in [15],[16],[18] have developed different flocking techniques, but with a common factor: being used for applications in environments with Global Navigation Satellite System (GNSS) denied environments, emphasizing the system's utility. Authors in [9] used the system for swarming models with the purpose of target capturing, relying on the UVDAR for the measurement and localization of its target and agents, allowing the interaction and decentralized behavior. The latest applications include the UVDAR-COM system for communication-challenged environments [8] and explicit communication in search and rescue applications [3], proving its viability against traditional systems such as GNSS and RF based communication.

- **System Model**

The UVDAR-COM system, is supported by its UV light-based TX and RX components. The TX utilizes UV LEDs to encode messages into binary frames for transmission of data. Simultaneously, the RX utilizes UV-sensitive cameras for decoding these messages, allowing accurate identification and tracking of UAVs.

Transmiter TX Unit

The optical transmitter architecture was designed to facilitate the optical communication, enhancing the system's ability to accurately and efficiently identify UAVs.

- **Binary Sequence Construction:**
  For the efficient identification of multiple UAVs, the development of binary sequences is an essential component of the system. Integrating the concepts of a dictionary (D), Non-Return-to-Zero (NRZ) coding, and unique sequence specifications to design a binary sequence with known properties to streamline its identification [4].
  - Applying NRZ coding to maximize the rate of bit transmission adapted for optical signals.
  - Setting the minimum average power and maximum continuous light emission requirements for the sequences for distinguishing between the designed binary sequences and environmental light sources.
  - Finally, encoding the signal through NRZ or Manchester to modulate with OOK produces the continuous-time electrical signal.

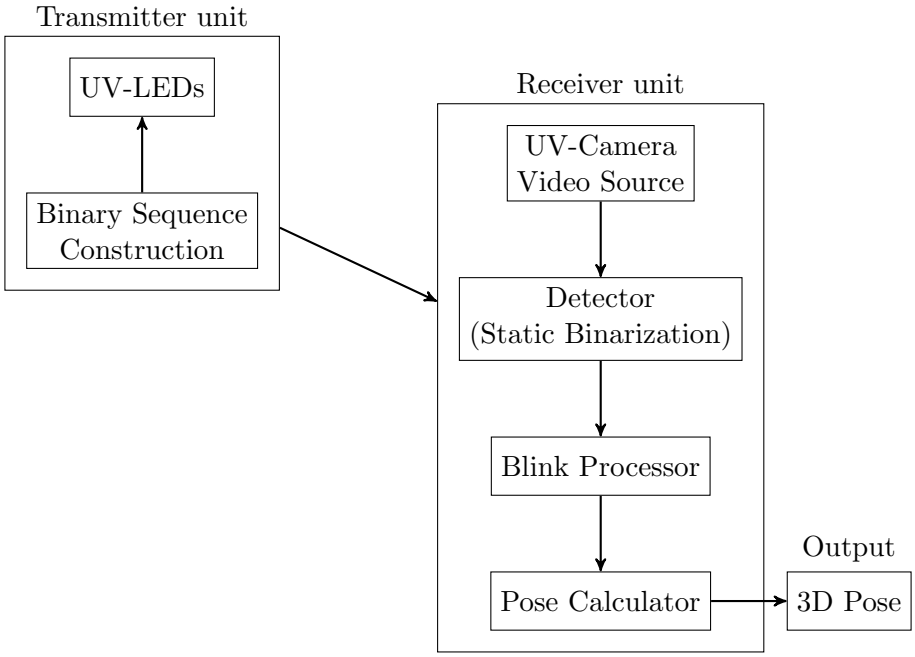

Figure 2.11: UVDAR Pipeline Overview.

- **Analog Frontend:**

  This component mainly represents the optical power that the UAV emits by converting the binary electrical signal into an optical signal. Two LEDs at each end of a UAV arm emit the same optical signal at a wavelength of 395 nm, which is in the UV spectrum. The LEDs are positioned in orthogonal orientations to improve the range at which the optical signal can be perceived [4].

Receiver RX Unit

The design has multiple components for properly handling the optical data transmitted by the LEDs on other UAVs.

- **Camera**

  The UAV is equipped with a grayscale camera and an UV bandpass filter. With a predetermined exposure time, capturing frames at every falling edge of the clock signal and synchronized for the recording of the changing LED states, ensuring the accurate identification of optical signals. [4]

(a) : Matrix Vision mvBlueFOX-MLC200wG camera module.

(b) : Sunex DSL215 fisheye lens.

(c) BP365-R6 bandpass filter

Figure 2.12: (a) mvBlueFOX camera (b) Fisheye lense (c) UV band pass filter.

- **Detector**

  Once the optical signals are captured, the image processing module has the main objective of identifying the bright spots emitted by the UV-LEDs in the captured images. In particular, the bright points are binarized by a using a an algorithm relying in static thresholding, performing a non-maxima suppression, this procedure similar to the Features from Accelerated Segment Test (FAST) with GPU acceleration to provide the set of (x, y) coordinates of the potential detected LEDs as well as potential sun points [5].

- **Blink Processor (Tracking)**

  The role of the blink processor module is to efficiently track and identify the blinking light sequences from UV-LEDs, and ensure the correct association of the blinking sequences with their respective UAVs. In particular, this is currently done by the Anonymous Blinking Marker trackIng (AMI) algorithm [1], a new method with superior performance in comparison with the previous 4D Hough Transform (4DHT) [37].

  - **Tracking:** Due to the intermittent presence and movement of these binary blinking UV LEDs in the observer's image, single-image computer vision approaches are insufficient. AMI addresses this issue by tracking the movement of these binary blinking markers over consecutive camera frames, utilizing a dynamic buffer to manage the tracking process.
  - **Correspondence Search:** AMI employs a local search to address the association problem of the corresponding UAVs and blinking markers, using a predefined expected search window derived from maximal expected movement. In case that the local search is unsuccessful, an extended search is employed to predict the next appearance of the marker using the previous image locations, designed for scenarios of complex movement like agile maneuvers.
  - **Verification:** Finally, a verification stage evaluates the sequences stored within the dynamic buffer. Upon successful correlation with a predefined sequence in the shared dictionary D, the algorithm confirms the UAV blinking sequence by providing the image coordinates (x, y) along with the matched ID, for further processing by the pose calculator.

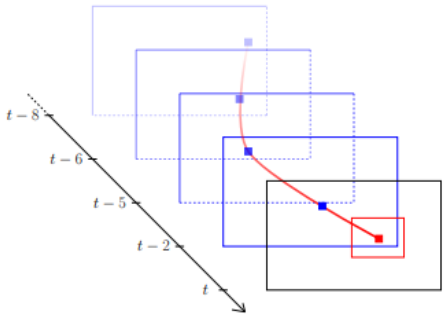

Figure 2.13: Image captured (blue), polynomial regression (red line), and search area (red rectangle) Fig. in [1].

It is important to note that the procedure may encounter difficulties such as LED occlusions, abrupt movements of the bright spots within the camera frame, or patterns that cause LEDs to turn off for extended periods of time [4].

- **Pose Calculator**

  This module select the most suitable fit from a set of randomized hypotheses regarding the pose that is reprojected into the image for comparison [31], Following this, the hypothesis is converted to a mean and covariance integrating bearing and distance estimation through the use of a linear Kalman Filter (KF) for pose estimation, and projection of relative pose using Unscented Transform (UT) [28].

  - **Pose estimation:** The linear KF improves reliability by handling instances where targets are occluded or exited the sensor's field of view, maintaining accurate pose estimations from the relative measurements, including covariances that approximate the measurement noise or reliability.
  - **Pose projection:** The process projects these relative pose estimates into bounding boxes around the target UAV camera image, using the UT-generating a projection of the position estimates and covariance, into the camera frame forming either rotated ellipses or rectangular areas.

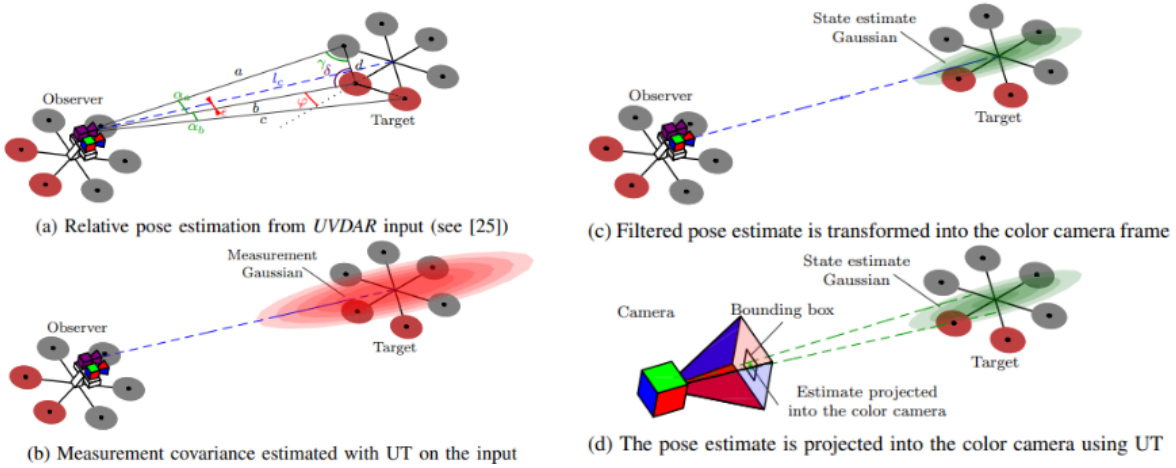

Figure 2.14: Pose estimation and projection UT Fig.4 in [28].

3 Problem Statement

Contents

3.1 Static Thresholding in Detection

When the UVDAR system is in its initial detection phase, the camera images are processed using a detection algorithm to identify potential UV LEDs, illustrated in Figure 3.1 image input with modified camera. For this purpose, it analyzes the pixels in the entire image to evaluate them against a defined static threshold. If the pixel is above the threshold value, examined with the circular segment test, and if identified as an LED, preserving only the highest value.

$$b(x,y) = \begin{cases} 1 & \text{if } g(x,y) > T, \\ 0 & \text{if } g(x,y) \leq T. \end{cases} \tag{3.1}$$

where the function $b(x,y)$ indicates the binary response defined for each pixel in the gray-scale image against the initialized threshold. This segmentation process reduces image complexity, facilitating the identification of UV optical signals emitted.

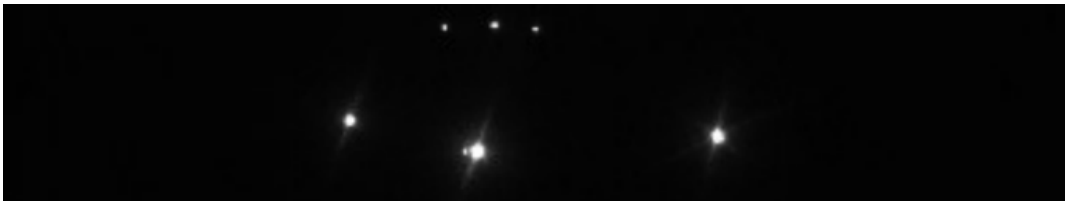

Figure 3.1: The image description, captured by the modified camera, shows two UAVs at varying distances, with "white" blinking UV indicators (Figure 6. in [38].

In the State-of-the-art (SOTA) detection algorithm, the intensity of each pixel is evaluated with a static threshold, if greater than this threshold it is evaluated to determine its potential as a marker point, if being brighter than its circular neighborhood, or as a sun point where surrounding pixels are brighter from the point. After going through the surrounding pixels, if a point still appears as a potential marker, the pixel with the highest intensity in the interior region, among the candidate and nearby pixels, is recorded as the detected marker, process illustrated in Figure. 3.2. Through this process, a single pixel known as a "white point" is created from several pixels representing the same bright spot, providing the spatial coordinates (x,y) coordinates and indicating the active ('on') state of a UV LED interpreted as a binary '1'.

This phase plays a crucial role in accurately tracking and decoding UV-LED signals used for UAV communication and localization, which is indispensable for ensuring the efficient operation of the UVDAR system.

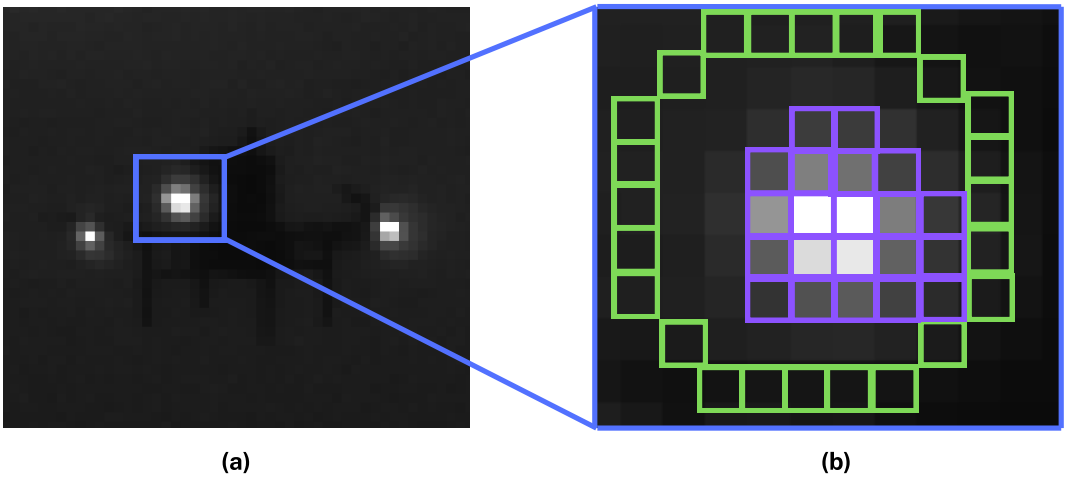

Figure 3.2: (a) Detail of a single UAV with 3 distinguishable isolated UV LED markers to be detected (b) Detail of a single marker for the circular segment test (green) and interior peak search (purple).

3.2 Current implementation limitations

Adapted for OCC, the UVDAR system may encounter difficulties as it was initially designed for mutual relative localization. Fundamental principles describe the characteristics of UV light and its reception, which presents significant aspects to address given its potential impact on communication effectiveness, justifying the need to optimize the system for the current task.

Intensity and Distance Challenges

According to the Inverse Square Law [43], the intensity of light observed from the UV markers diminishes quadratically with increasing distance from the receiver:

$$\text{intensity} \propto \frac{1}{\text{distance}^2} \tag{3.2}$$

Consequently, signal intensity decreases significantly over longer distances, as illustrated in Figure 3.3, complicating the accurate decoding of transmitted data at increased distances.

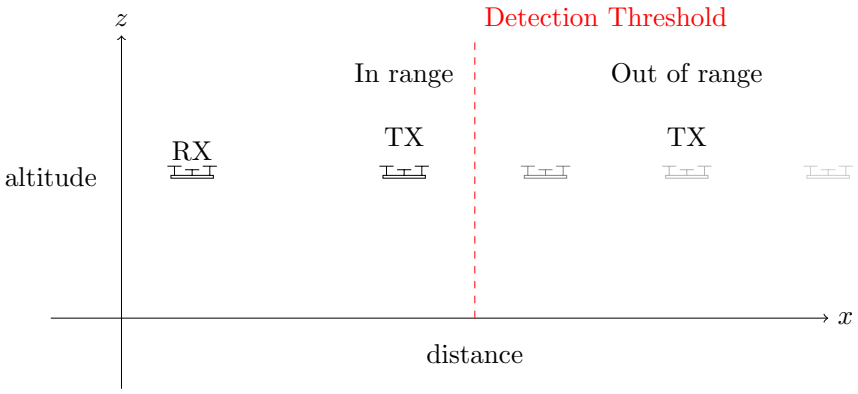

Figure 3.3: Scenario where static binarization leads to undetectable levels despite RX UV LED visibility. TX signal strength decreases with distance, following the Inverse Square Law.

In conjunction with prior research conducted on UVDAR [38] regarding the relationship between distance, bright spot size, and exposure impact. In Figure 3.4 the vertical lines indicate the point of reduction to a single pixel. Highlighting the comments by the author on the selection of exposure time, selecting short exposure times would increase the accuracy of the system but would lead to operating at short distances, whereas choosing a long exposure time would increase the operating distance at the expense of reducing the performance by having less selectivity w.r.t. other light sources.

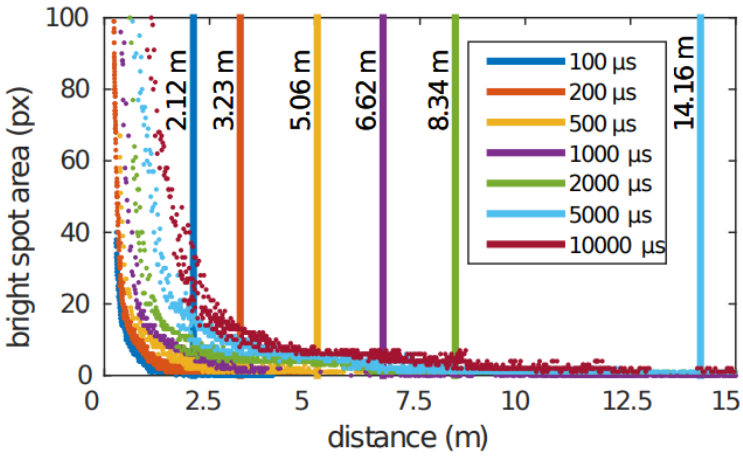

Figure 3.4: Bright spot size distance dependence. Fig.10 in [38].

Angle of Incidence and Reception

Another source of difficulty is introduced by the system's dependence on Lambertian radiation characteristics for UV LEDs, as dictated by the Lambertian cosine law that the UV LEDs are expected to follow [38]:

$$I(\theta) = I_{\max} \cos \theta \tag{3.3}$$

The observed light intensity is directly proportional to the cosine of the angle between the observer's LoS and the direction in which the LED is pointing, Figure 3.5 displays an ideal lambertian source and angle effect. As a result, the radiation intensity decreases to less than half its maximum value when the viewing angle is more than sixty degrees. This reduction in signal strength at non-perpendicular angles restricts the effective field of view within the UAVs that can reliably receive signals, potentially imposing more demanding alignment between transmitter and receiving units for optimal signal retrieval, example illustrated in Figure 3.6 .

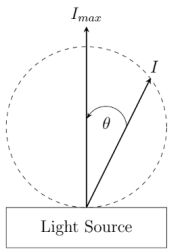

Figure 3.5: Ideal lambertian Source Model and angle dependency.

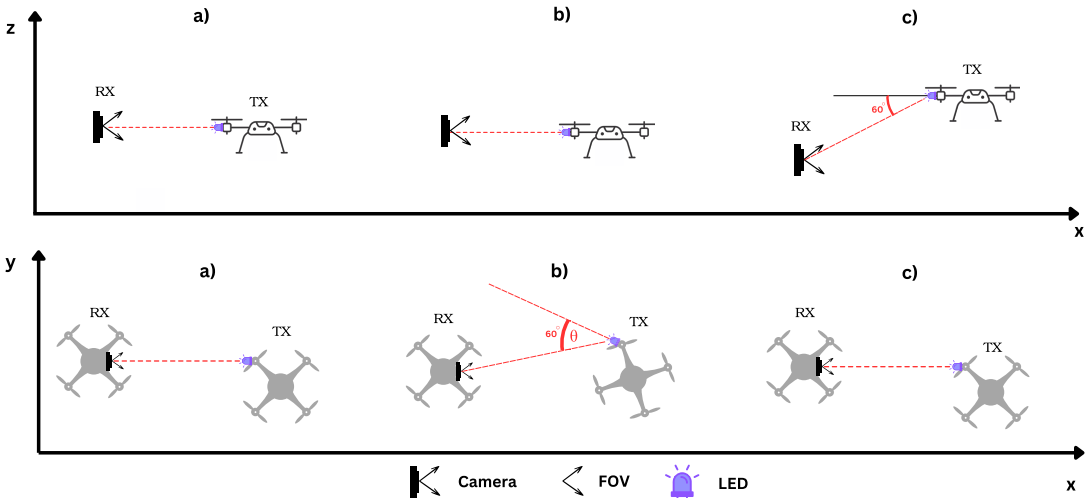

Figure 3.6: (a) Angle of departure 0 degrees (b) Angle of departure of 60 degrees (Azimuth Angle) (c) Angle of departure of 60 degrees (Angle of elevation).

Understanding the signal attenuation within the UVDAR system necessitates considering the effects of the distance and the angular orientation. The combined effect of the Inverse Square Law and the Lambertian cosine law allows us to understand their impact on signal intensity:

$$I(d, \theta) = \frac{I_{\max} \cos \theta}{d^2} \tag{3.4}$$

By considering these principles, we can formulate more realistic operational scenarios for the UVDAR system. Demonstrating the necessity of the system being capable of dealing with the intrinsic effects of optical attenuation to enhance its reliability and efficiency.

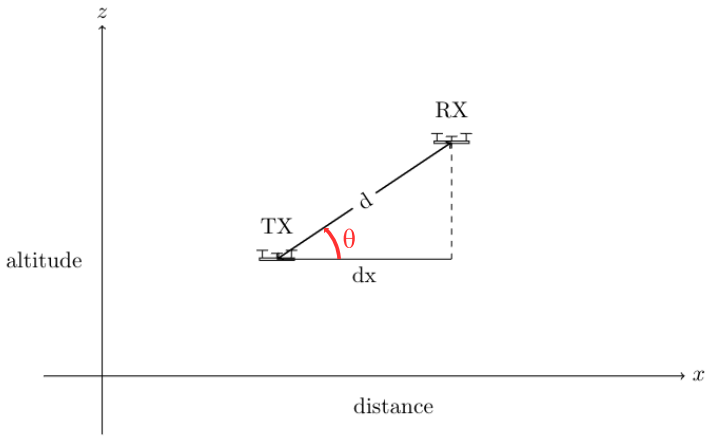

Figure 3.7: Dual consideration of Inverse Square Law and Lambertian Cosine Law.

System Design and Communication Range

UVDAR's initial design did not incorporate communication capabilities, meaning the current architecture might not optimally support these tasks. For instance, variations in signal strength that the static threshold for detection does not account for, affect the range of communication. Additionally, problems could arise by using circular neighborhood separation in the detection mechanism, leading to inaccuracies in situations where multiple LEDs are nearby. Erroneously identifying a single marker, despite the fact that these LEDs do not converge into a single entity, as shown in Figure 3.8. This situation in the camear appears in scenarios of headings towards the RX with minimal separation between the LEDs, as shown in Figure 3.9.

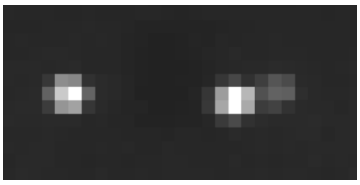

Figure 3.8: Grayscale image of UAV at 15m from RX

This identification error of close LEDs is more likely to occur in dense LED arrangements in multi-robot operations, or long-distance scenarios with a pair of UAVs coming close

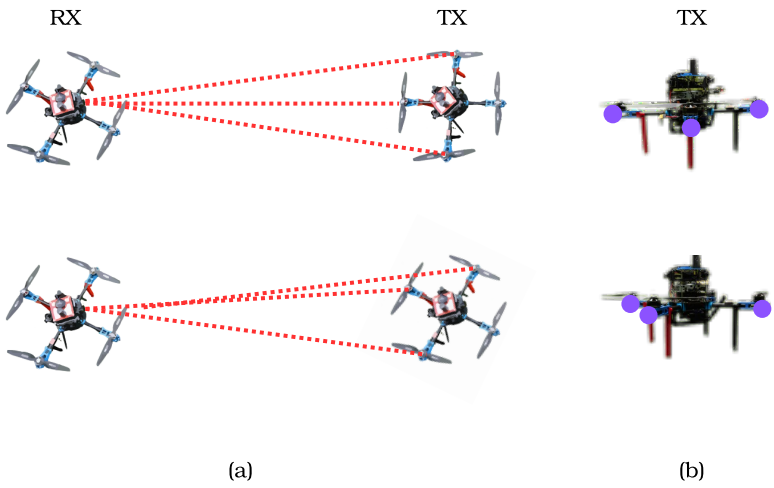

Figure 3.9: (a) Top view of LoS between RX and TX, first a heading with maximal separation between LEDs, second a scenario with heading with minimal separation. (b) Orthogonal view of TX with respect to RX.

together, where the precision of individual marker detection is significant, having unique signals coming from various LEDs and UAVs.

Moreover, the system's scalability and flexibility are limited in a complex operational scenario of multiple UAVs with varying distances and orientations due to its inability to adapt to the changing intensities of signals from different UAVs. These physical and system-based limitations highlight the need for substantial enhancements in the system to support robust and reliable optical communications expanding the system's utility for various UAV applications.

The results of the UVDAR-COM validation where donde by the authors in [11], shown in 3.10, where the BER analysis of the system showed stable conditions up to 17 meters. Additionally, BER would be degraded at close distances due to the possibility that the image elements are too large for the circular neighborhood in the detector. As the circle simultaneously incorporates both, the algorithm is accountable for the merging of the nearby points. Furthermore, the tracking for blinking extraction utilizes image positional data to determine the temporal association of markers, which, if the points are that close, will connect the adjacent points.

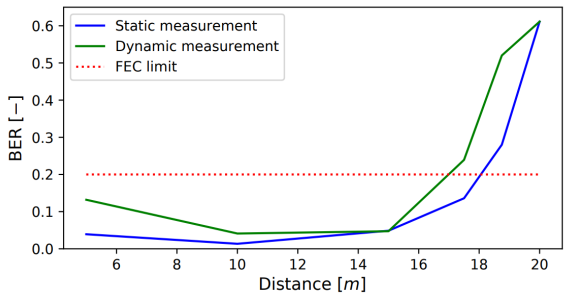

Figure 3.10: Dependency of BER on the mutual distance between UAVs, Fig.9 in [11].

3.3 Analysis of the UVDAR datasets

Understanding the nature of pixel intensity at various distances was necessary to address the current limitations. The data for the analysis was collected using video recordings made by the team during previous experiments, the datasets correspond to experiments performed with different distances and exposure configurations. The recordings used for the online execution of the UVDAR, using the tracking algorithm to obtain the position in the image corresponding to the UV-LED to extract grayscale value in the image.

Given camera frame drops present in the experiment recordings, to avoid mismatches from the tracking and the image positions, Max pooling was employed to guarantee obtaining the pixel with the highest intensity, ensuring the accuracy of the data to analyze.

Details of the experiments

The experiment datasets consist of 1 RX and 2 TX, with trajectories designed for the UAVs to stay in position while maintaining relative distance. Setting the RX in a static position with one camera pointing towards the TXs. One TX was kept approximately 3–4 meters w.r.t the RX in all experiments, and the other TX varied its distance throughout the experiments at 5, 7, 10, 15, and 18 meters. For both TXs, the L12 sequences was used with a normalized power of 0.5, meaning each sequence will have the same number of values of 0 and 1. These sequences are shown in Table 3.1

ID	Sequences
1	0, 0, 1, 0, 0, 1, 0, 1, 0, 1, 1, 1
2	0, 0, 1, 1, 1, 0, 1, 0, 1, 1, 0, 1
3	0, 0, 0, 1, 1, 1, 0, 0, 0, 1, 1, 1
4	0, 0, 0, 1, 0, 0, 1, 1, 0, 1, 1, 1
5	0, 1, 1, 1, 0, 1, 1, 1, 0, 1, 1, 1
6	0, 0, 1, 1, 0, 1, 1, 0, 1, 0, 1, 1
7	0, 0, 1, 0, 1, 1, 0, 0, 1, 0, 1, 1
8	0, 0, 1, 1, 0, 1, 0, 0, 1, 1, 0, 1
9	0, 0, 0, 1, 0, 1, 0, 1, 1, 0, 1, 1
10	0, 1, 0, 1, 0, 1, 0, 1, 0, 1, 0, 1
11	0, 0, 1, 0, 1, 1, 1, 0, 0, 1, 1, 1
12	0, 0, 0, 1, 1, 0, 0, 1, 1, 1, 0, 1

Table 3.1: L12-P0.500000 Blinking Sequences [4].

The experiments were conducted in the desert of Abu Dhabi, and in particular, it was a challenging scenario because the camera of the RX was pointing towards the sun. In the figure, An image of the scene is illustrated in Figure 3.11, showing a large amount of light present in the image. Sequences 7 and 5 were selected for the TX that increases its distance from the RX and the TX that stays close to it throughout the experiments.This distinction is valuable for conducting the analysis, obtaining directly from the tracking algorithm the TX position of the image with its emitted sequence.

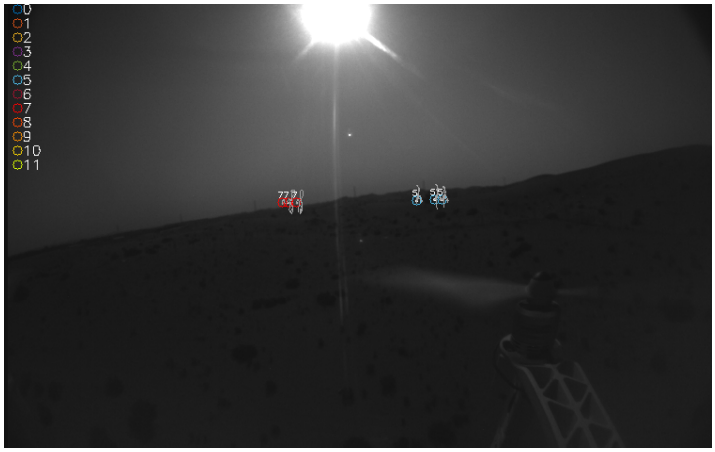

Figure 3.11: UVDAR Vizualization: TX (Signal 5) in blue marker on right and TX (Signal 7) in orange marker on left.

We obtain the Probability Mass Function (PMF) and Cumulative Distribution Function (CDF) to visualize the data distribution since this information allows us to analyze it with histograms. A range of low- and high-intensity ranges are present, as the tracking provides the positions of both states of the LED.

Given distributions would also be dependent on the threshold used for the execution online, the data was extracted by setting thresholds of 150, 100, and 50 to analyze its influence.

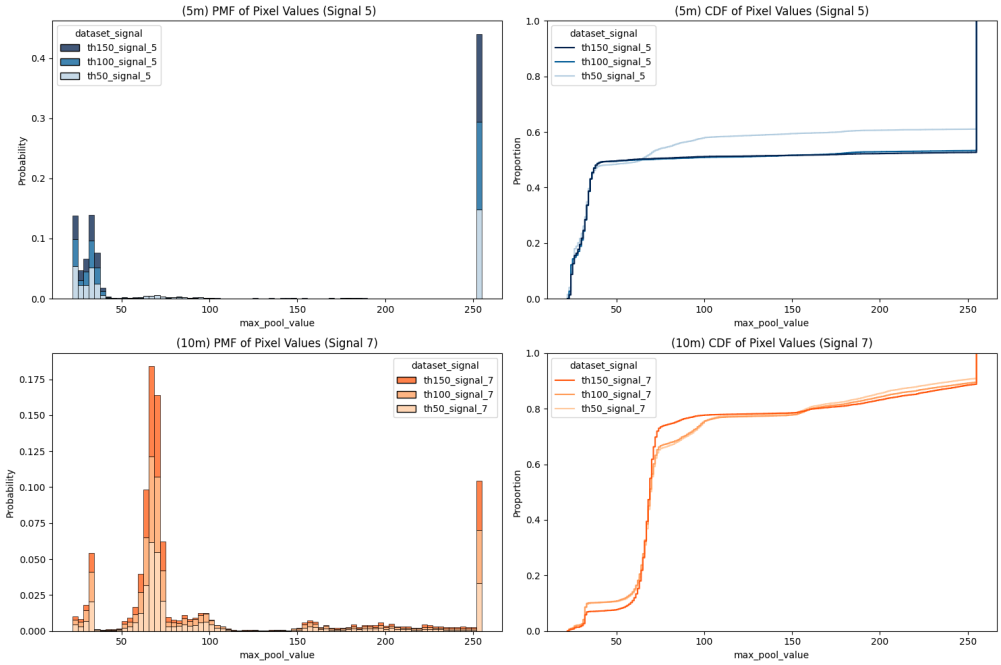

Figure 3.12: PMF and CDF from TX (Signal 5) at 5m and TX (Signal 7) at 10m.

In the PMF of the shortest distance at signal 5, we observe that most of the ON values are in saturation, as seen in Figure 3.12. However, at signal 7, the peak of the saturation values is smaller, with a higher variance between the values starting from 150. At short distances, the distributions in proportion are similar, which is confirmed by the CDF, and with increasing

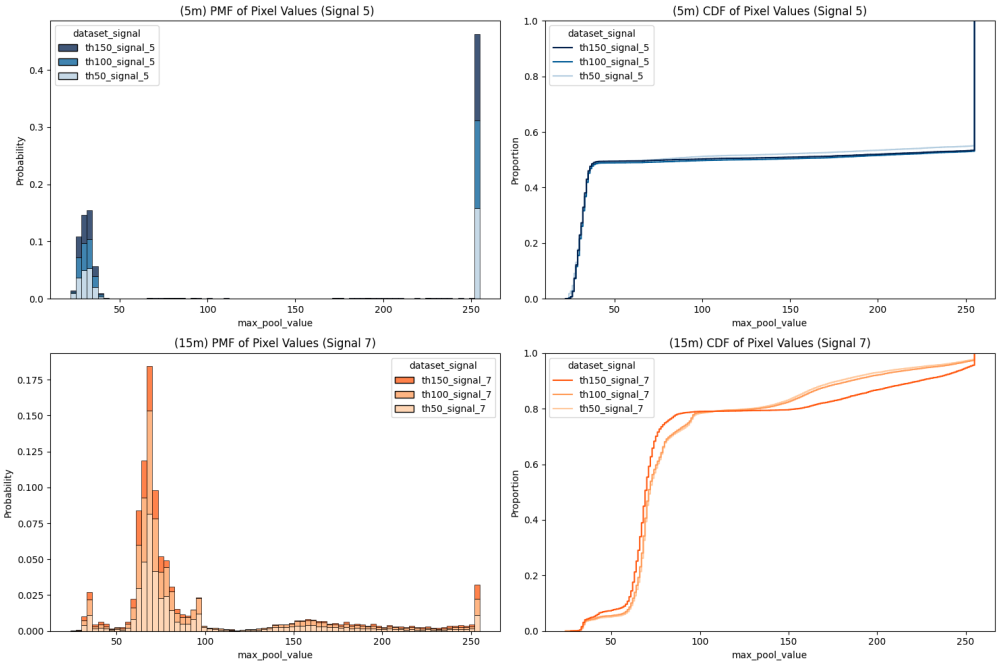

Figure 3.13: PMF and CDF from TX (Signal 5) at 5m and TX (Signal 7) at 15m.

distance, the saturation values decline with the central tendency moving towards 150 at 15 meters, illustrated in Figure 3.13.

As previously indicated by the inverse square law, from the points received with the LED State ON, its mean pixel intensity decreases with increasing distance. The trend with increasing distance is presented in the following Figure 3.14.

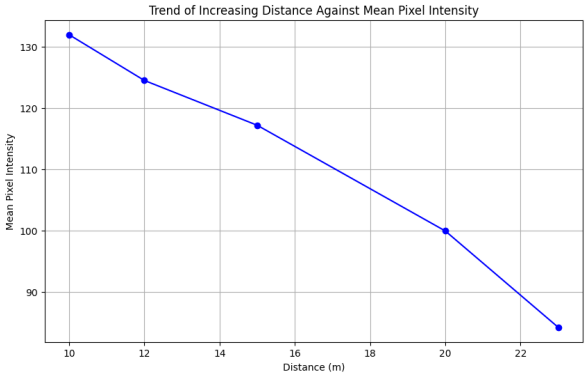

Figure 3.14: General Mean Pixel Intensity with increasing distance.

At a distance of 20 meters (Figure 3.15), the values of 150 and 100 are less frequent compared to the threshold of 50, with most of the values being below 150 at the given distance. At 23 meters (Figure 3.16), the threshold of 150 completely loses the signal, while the threshold of 50 remains, remaining unaffected by the LED pixels' low intensity.

Up to 20 meters, the detected points with a threshold of 50 is about five times more than the 100 value, and 15 times more than the 150 value. However, at 23 meters, the performance of the 50 and 100 thresholds is similar. Appendix A contains the statistical data categorized by signal and distance.

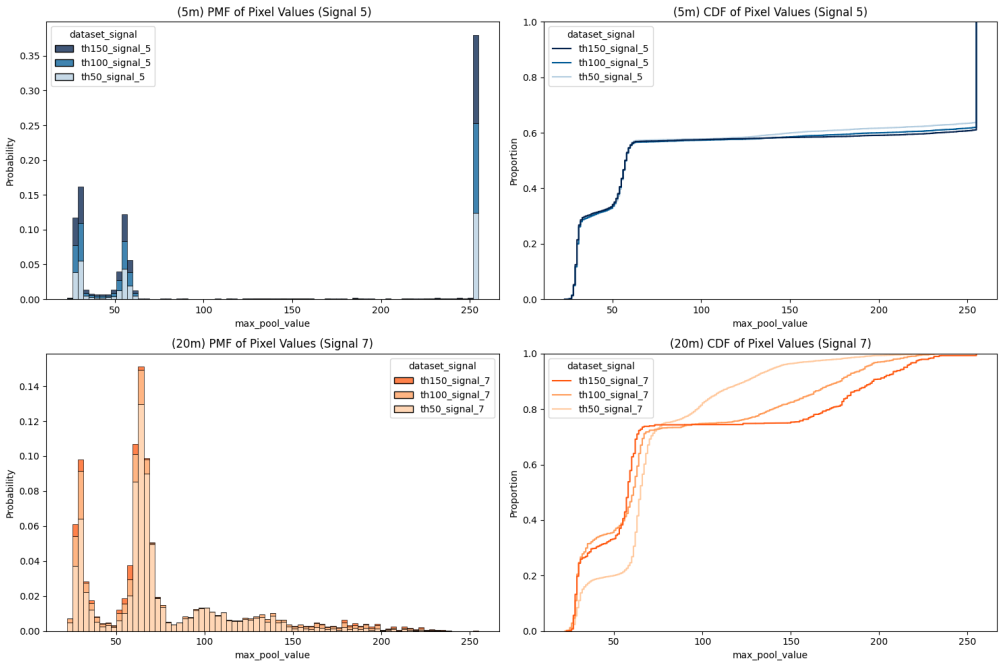

Figure 3.15: PMF and CDF from TX (Signal 5) at 5m and TX (Signal 7) at 20m.

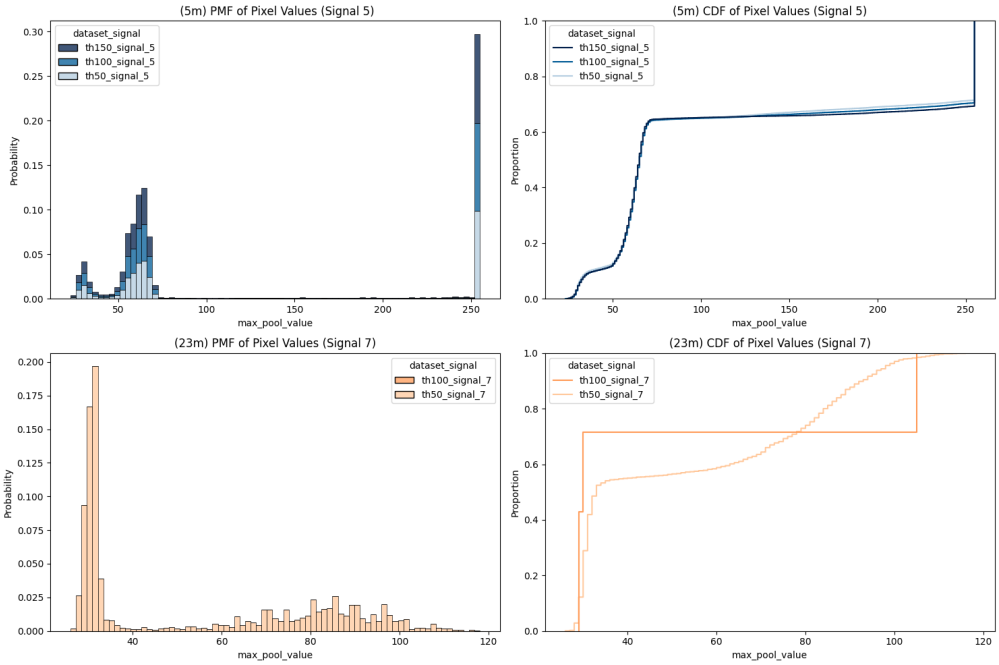

Figure 3.16: PMF and CDF from TX (Signal 5) at 5m and TX (Signal 7) at 23m.

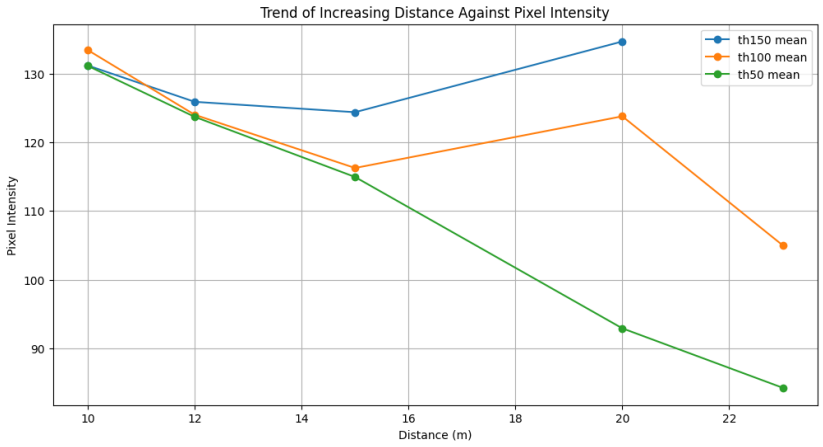

Figure 3.17: (Signal 7) Mean Pixel Intensity for LED State ON with increasing distance.

It is important to note that the obtained results align with previous findings from [11]. Whereas in Figure 3.10 we observed, the BER is stable up to 15m, what we also observed in our trend is the point where the decrease begins, illustrated in Figure 3.18. It should be mentioned that within the 10-15 meters range, the detection count is increasing, which may be biased due to the extraction process or the duration of each experiment, as there are variations between the movements at the beginning and end of each experiment. However, it is consistent with figure 3.10, where the BER decreases until 10 m, with the same decline in detections at 15 meters.

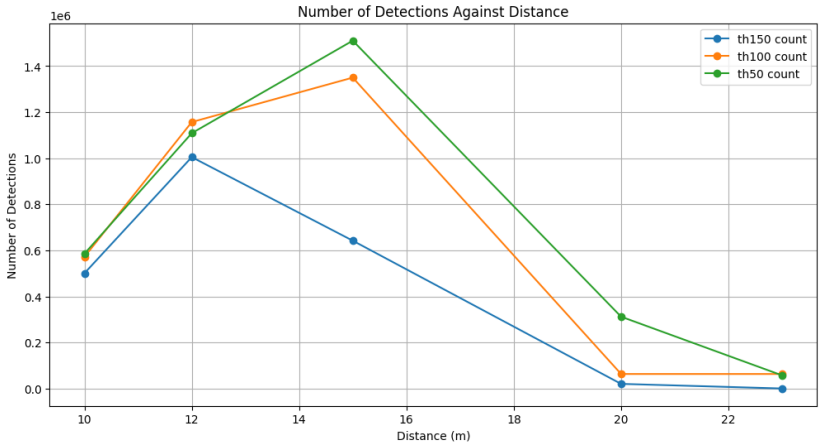

Figure 3.18: (Signal 7) LED State ON occurrences with increasing distance.

We assume this is where the distance starts to affect the detection since the trend graph of the average pixel (from Figure. 3.14 intensity values around 15 meters starts to get close to 100, which in grayscale means a medium to light gray tone, as illustrated in the grayscale scale palette, shown in Figure 3.19, with several intensity values.

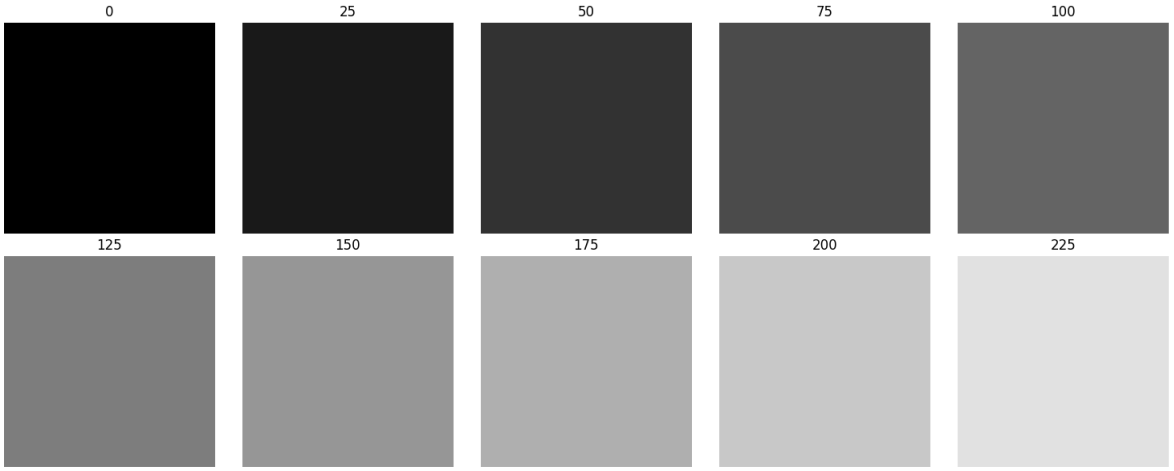

Figure 3.19: Gray-scale pixel values palette.

Therefore, one factor potentially affecting detections at long distances is that the image of the LED appears darker (passing from white at short distances to shades of gray at longer distances) which may make it more challenging to identify this point as it dissipates with gray tones in the background, an example in Figure 3.20 where with LED in gray tones similar to background.

In terms of results, we can confirm that a lower threshold achieves higher occurrences for the signal decoding, representing a higher communication range. However, referring back to the author [38], selecting a lower threshold would increase the operating distance while affecting the system precision. Therefore, one of the goals we aim to achieve with the adaptive threshold is to eliminate the constraint of finding the balance between accuracy and operating distance, motivating us to find better strategies to adapt to lower intensity to improve the system capacity.

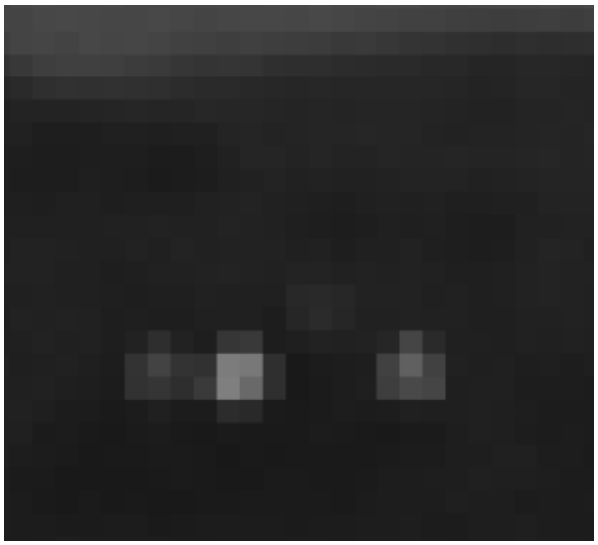

Figure 3.20: Background dissipation.

4 Adaptive Thresholding algorithm

Contents

4.1 Motivation for Adaptive Approach

Although implementing static binarization in the UVDAR system is the fastest solution it also limits its performance. Careful consideration needs to be given to its initialization, which is crucial for ensuring proper operation and overall success. For instance, the background noise can be reduced by selecting a high threshold, but compromising the ability to detect UAVs at medium or long distances despite the visibility of the LEDs in the grayscale image, as shown in Figure 3.3. On the other hand, by choosing a low threshold to increase the detection range still will be inherently constrained for only values above this threshold.

Additionally, in scenarios with multiple UAVs, as illustrated in 4.1, we can have both UAVs at long and short distances simultaneously, making it insufficient to use a single threshold value, motivating for better strategies.

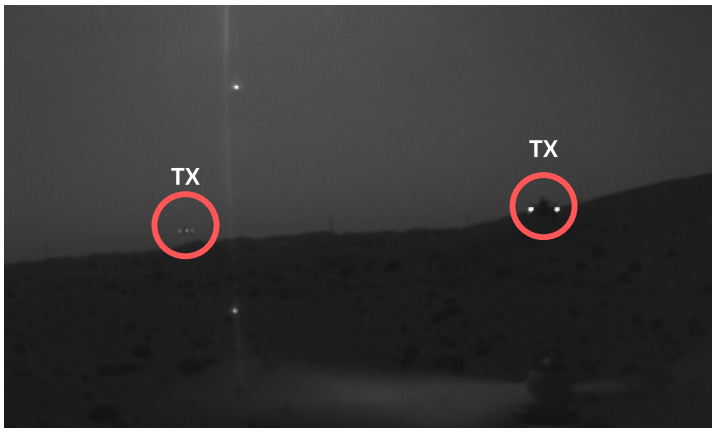

Figure 4.1: Multiple TX in camera image

An adaptive detection approach presents a solution by dynamically adjusting thresholds. Our goal is to enhance the system's robustness and adaptability, making it a more reliable option for a range of UAV applications.

4.2 Adaptive Thresholding Algorithm

In this thesis, an adaptive thresholding algorithm for the UVDAR system is proposed. This algorithm uses feedback from the tracking algorithm to determine where UV LED markers are present. The objective of this mechanism is to concentrate the binarization on the ROIs where our LEDs are expected to be.

Utilizing an adaptive approach to analyze the entire image would increase computational demand and increase noise, as observed in 4.2, having a greater likelihood of segmenting bright regions or objects present in the image. As a result, the proposed method avoids this challenge by focusing on small ROIs.

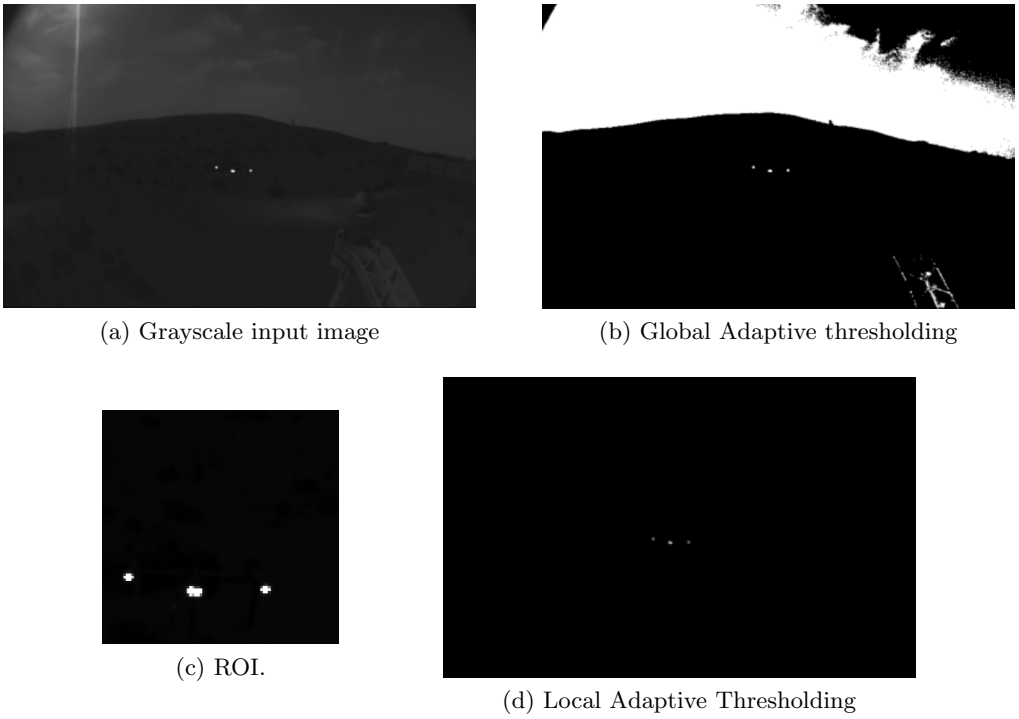

(a) Grayscale input image

(b) Global Adaptive thresholding

(c) ROI.

(d) Local Adaptive Thresholding

Figure 4.2: Comparison of global and local adaptive thresholding.

As previously mentioned, detecting multiple UAVs with different distances can affect signal integrity by binarizing multiple UAVs simultaneously with a single threshold. With various pixel intensities, we cannot guarantee proper decoding for each. Therefore, by assigning an ROI for each UAV present in the image and separately processing them, we aim to improve the detection of our UV LED signals, consequently optimizing its capabilities.

4.3 Overview of the adaptive approach

The adaptive processing had been designed to be integrated into the system using the current modules, building upon them to accomplish our task. Given the need for feedback to begin with adaptive processing, the system operates under standard conditions to obtain this information from the tracking module, starting by employing the SOTA detection method using the static approach. This to initially identify the bright points in the image, and then allowing the construction of ROIs for adaptive processing.

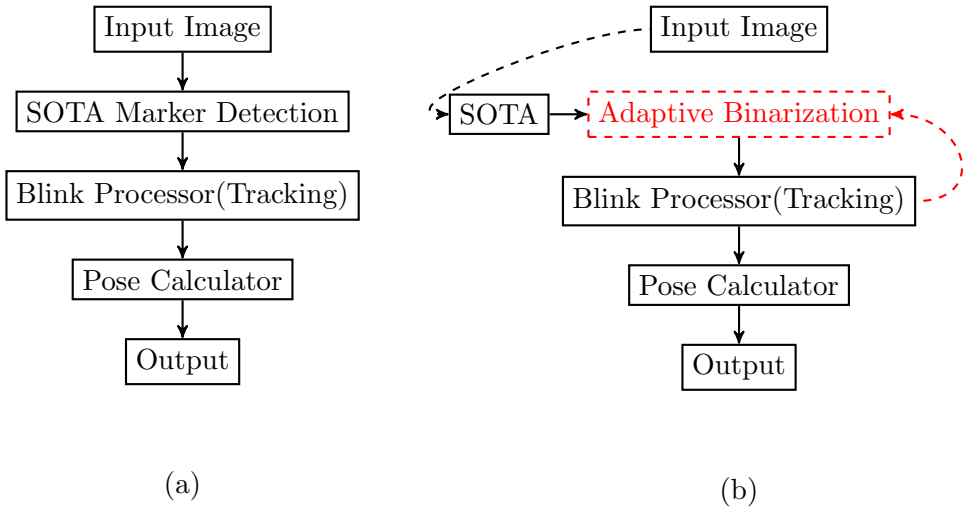

(a) (b)

Figure 4.3: (a) Overview of the current UVDAR modules (b) Integration of the Adaptive Binarization.

Pseudocode

(i) Start **static binarization** processing of the image.
  (a) Get initial **detected points**.
(ii) If received feedback from tracking:
  (a) Calculate the **ROI** around the provided points.
  (b) Find overlapping **ROIs** and calculate **MergedROIs**.
  (c) Get final **ROIs** to be processed.
  (d) Apply **adaptive thresholding** to the final **ROIs**.
  (e) Calculate the **centroids** of adaptive detected points.
  (f) **Merge** with initial detected points, giving priority to adaptive points.
  (g) Return the potential detected points.
(iii) If we stop receiving information from tracking, go back to **step i**.

The static detection method was preserved as a baseline for the rest of the process due to the complexity of initially processing the whole image adaptively and obtaining the points of interest without over-segmenting the image and introducing noise as mentioned before. Besides, the static detection method is optimized for GPU parallel processing, making it a viable option as it does not add more computational load on the CPU.

In situations where the adaptive process fails to accurately identify the points of interest, it additionally functions as a fallback, capitalizing on the strengths of both approaches; static processing is a fast and efficient way to make the initial detection of points, while the adaptive method ensures more accurate processing addressing the limitations of static processing.

The development of the adaptive algorithm involved the implementation of adaptive thresholding methods as well as the design of several mechanisms to optimize the process and to guarantee an improved segmentation result based on our needs. These mechanisms include ROI evaluation processes to determine overlaps between each other as well as pre-and post-processing of our ROI. The following section provides detailed descriptions of these and additional techniques.

Adaptive Algorithm

Algorithm 1 Processing of image adaptively

Input: I, **T**, **S** ▷ Input image **I**, Set of tracking points **T**, Set of static points **S**
Output: D ▷ Set of detected points **D**
if **T**.size() == 0 ∨ **T**.size() ≥ MAX ROIS **then**
    return False
end if
R ▷ Set of ROIs, **R**
for p_i in **T** **do** ▷ Calculate bounding boxes
    $r_i \leftarrow$ **calculateROI**(p_i)
    R.append(p_i) ▷ Add bounding boxes to set **R**
end for
M ← **mergeOverlappingROIs**(**R**) ▷ Check overlapping **R**, Merged ROIs **M**
for m_i in **M** **do**
    D ← **applyAdaptiveThreshold**(m_i) ▷ Apply adaptive threshold to ROI m_i
end for
D ← **mergePoints**(**D**,**S**) ▷ Merge adaptive **D** with static **S** points
return True

4.4 ROI Adaptive Processing

ROI Merging

To minimize computational expense and streamline the process, we reduce unnecessary computations in cases where multiple points come from the same UAV, or when UAVs are close to each other. In these scenarios, overlapping ROIs may process the same image position and the same points from the same UV LED, complicating the process both by increasing computational load and making it difficult to distinguish between points from different ROIs.

Algorithm 2 Merge overlapping ROIs

```
Input: R                                              ▷ Set of ROIs
Output: M                                             ▷ Set of merged ROIs
M                                                     ▷ Initialize set for merged ROIs
m                                                     ▷ Initialize boolean set for merged ROIs
for r_i in R do                                       ▷ Current ROI r_i
    for r_j R do                                      ▷ Subsequent ROI r_j
        if isOverlapping(r_i,r_j) then
            c ← collectCorners(r_i,r_j)               ▷ Collect corners
            r_i ← boundingRect(c)                     ▷ Update current corners
            m[j] = true                               ▷ Mark r_j as merged
        end if
    end for
    M.append(r_i)                                     ▷ Add r_i to merged set
    m[i] = true                                       ▷ Mark r_i as merged
end for
    return M                                          ▷ Return set M
```

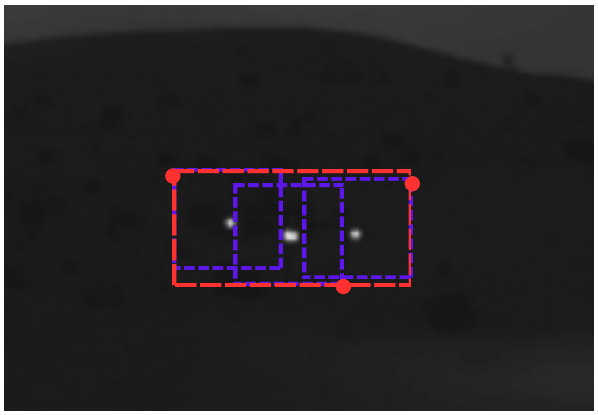

Figure 4.4: The ROIs, represented by dashed purple lines, are created according with each tracking point obtained. A red dashed line indicates the relevant corners used for merged ROI result.

Thus, when obtaining points from the feedback of the tracking module, ROIs are calculated based on previously areas. Areas covered by the resulting ROIs are evaluated, and if overlaps are found, they are replaced by a single ROI encompassing the involved areas, optimizing subsequent computation, process illustrated in 4.4.

- **Image Enhancement: Unsharp Masking**

To facilitate the process of detecting the bright spots corresponding to a UV LED within our ROI, and for enhancing the object to remain in the image after segmentation, a sharpening process was implemented. This process identifies the high-frequency components of our ROI to obtain an improved image, where more priority is given to our particular signal. It is homologous to and inspired by classical signal processing techniques, specifically high-pass filters, but adapted to image processing.

The process consists of a combination of Gaussian Blur and unsharp masking to highlight the borders in the image [47]. The blurring technique is applied to the original ROI using a Gaussian function to smooth out the image by removing the high-frequency components. This smoothed image is then subtracted from the original image, resulting in our unsharped mask representing the high-frequency components lost during the smoothing process, as demonstrated in 4.5. Finally, this detailed mask is added to the original image using a scaling factor. This factor controls the intensity of the sharpening effect, assigning higher priority to sharpening and enhancing high-frequency components.

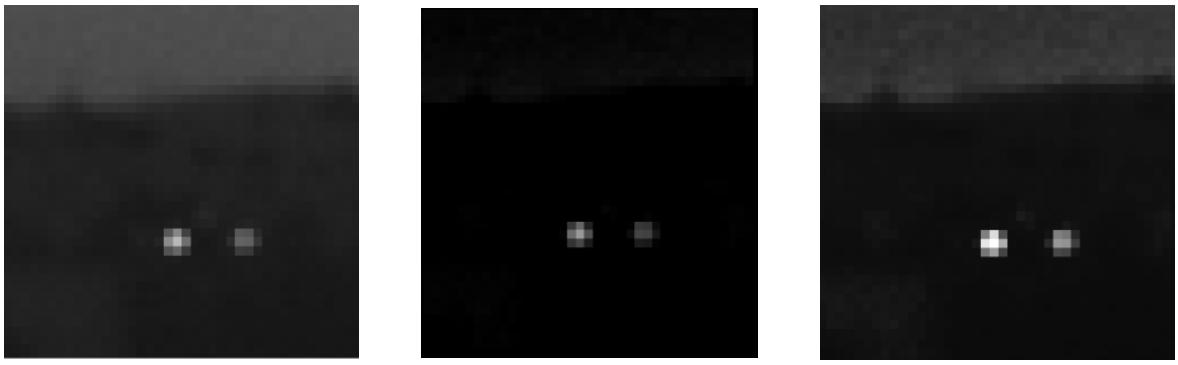

(a) Original ROI (b) Unsharp Mask (c) Enhanced Image

Figure 4.5: Image enhancement process

$$ROI_{\text{enhanced}} = \alpha \cdot (ROI_{\text{original}}) + \beta \cdot (ROI_{\text{original}} - ROI_{\text{blurred}}) \tag{4.1}$$

This process facilitates the identification process by attenuating the ROI background, ideally preserving bright spots present in our ROI, offering us the flexibility to adjust the values of α and β to facilitate the assignment of greater priority to high-frequency components.

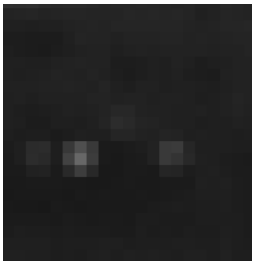

(a) Original ROI

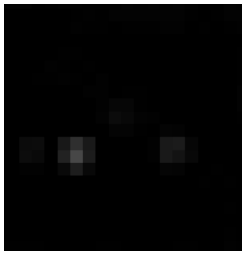

(b) Unsharp Mask

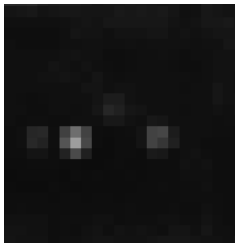

(c) Enhanced Image

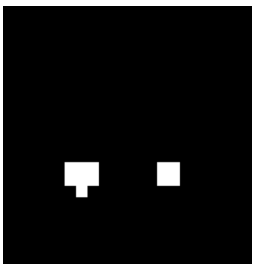

(d) Binarization result with Sharping

(e) Binarization result without Sharping

Figure 4.6: Binarization results comparison

This process is important for scenarios where the pixel intensity distribution is close to uniform or in scenarios with values comparable to our points of interest, complicating finding an optimal separation threshold, as demonstrated in Figure 4.6 with an example of a unsuccessful segmentation of our points of interest given low pixel intensity values at a far distance. The goal is to improve the image at the pixel intensity distribution level, moving closer to the ideal scenario of a bimodal distribution with distinct peaks and clear differentiation between low and high-frequency values, streamlining the process of segmentation given the background attenuation, as illustrated in Figure 4.7 having an enhanced ROI with the UV LEDs preserved and minimized the influence of the background.

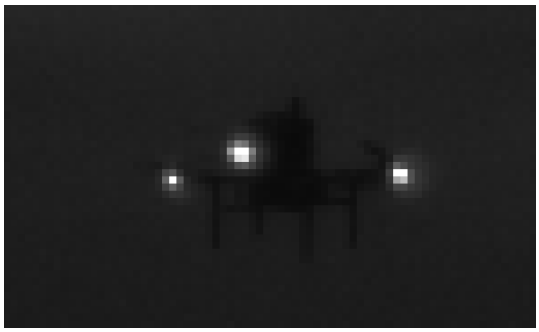

(a) Original ROI

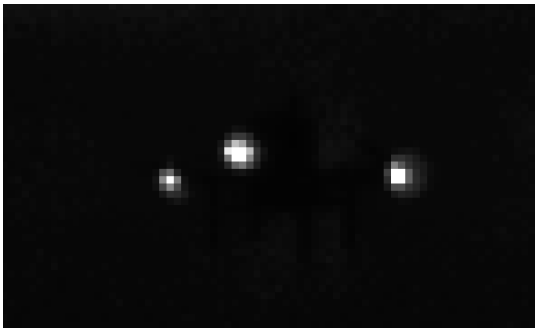

(b) Enhanced ROI

Figure 4.7: Example of high-frequency components preserved while enhancing.

The following example is an extreme case corresponding to a sun point reflection to demonstrate and visualize the effect of the enhancement process visually and at the histogram level. Observing in Figure 4.8, the original ROI histogram values corresponding with a background of medium intensity values before the enhancement, the enhanced ROI histogram values demonstrate the significant reduction of these medium frequency components, after enhancing, while the bright spot is maintained.

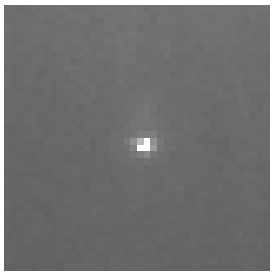

(a) Original ROI

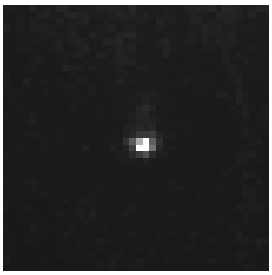

(b) Enhanced ROI

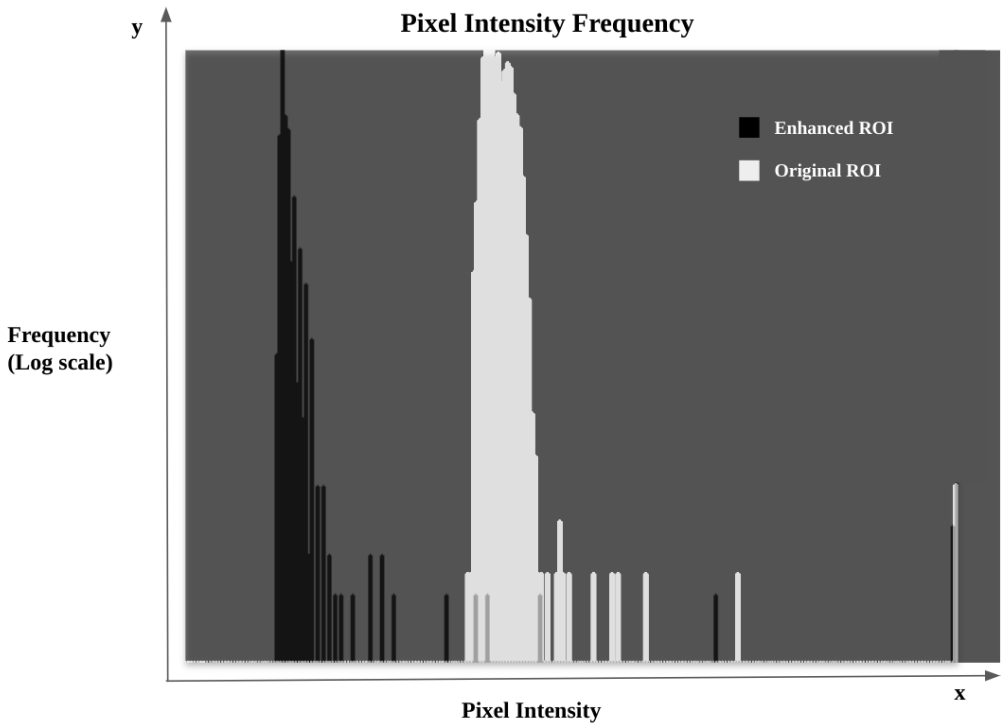

(c) Pixel Intensity Frequency comparison

Figure 4.8: Image and histogram before and after enhancement.

- **Area Filtering**

Subsequently, when applying the adaptive technique to the ROI and obtaining a binary image, post-processing techniques are performed to guarantee the candidate points correspond to UV LEDs. Due to the complexity of fully isolating bright spots from the image background when contrasting backgrounds are present, these are usually retained in the image. Therefore, to eliminate these easily distinguishable areas that do not correspond to a potential UV-LED, we applied Connected Component Analysis (CCA) on the ROI to categorize the areas that were segmented, retaining only the points that potentially belong to a UV LED in our ROI.

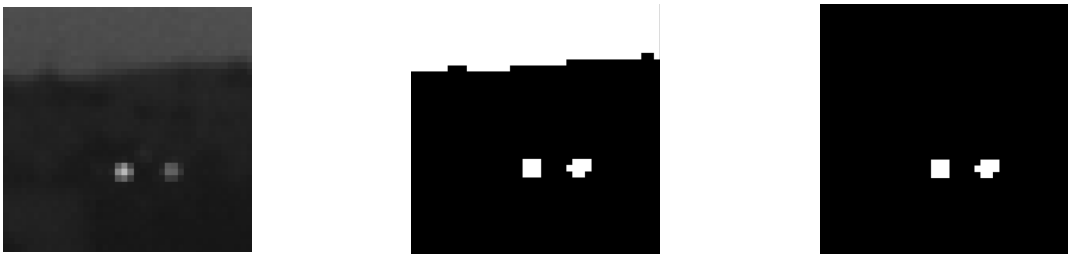

(a) Original ROI (b) Unfiltered Binary ROI (c) Filtered Binary ROI

Figure 4.9: Area filtering process

- **ROI Processing Algorithm**

Algorithm 3 ROI Processing

Input: R ▷ ROI
Output: D ▷ Set of detected points, **D**
E ← **enhanceROI**(**R**) ▷ Unsharp masking of **R**, Enhanced ROI, **E**
if "Otsu" **then**
    B← **findOptimalThresholdOtsu**(**E**) ▷ Obtain Binary ROI, **B**
else
    B← **findOptimalThresholdKL**(**E**)
end if
C ← **findContours**(**B**) ▷ Find contours in **B**
if **C**.size() ≥ MAX CONTOURS **then** ▷ Return empty **D**
    return D
end if
for c_i in **C** **do** ▷ Area filtering
    area ← **contourArea**(contour)
    if area < MAX AREA **then**
        m ← **drawContours**(c_i) ▷ Add contour to mask, **m**
    end if
end for
B ← **B** ∧ **m** ▷ Apply **m** to **B**
D ← **detectPointsFromRoi**(**B**) ▷ Detect points in **B**
if **D**.size() ≥ MAX DETECTED POINTS **then**
    return D.clear() ▷ Skip noisy **B**
else
    return D ▷ Return detected points from **B**
end if

4.5 Adaptive Threshold Methods

During the development of the project, different adaptive techniques were evaluated to fulfill the segmentation function of our ROIs. In particular, two methods were implemented: Otsu's method [48], responsible for finding the threshold with the best separation between foreground and background, and Kullback-Leibler (KL) Divergence minimization [49], which obtains the threshold with the lowest information loss.

Otsu's Method

Otsu's method is a popular technique employed for adaptive image thresholding. The goal is to separate the foreground (objects of interest) from the background using the gray scale histogram of the image and finding an optimal threshold value that separates these two regions with maximum between-class variance.

Algorithm Description

(i) **Compute the Histogram :**
Initially the histogram $H(i)$ of pixel intensities in the grayscale image is calculated, representing the frequency distribution of pixel intensities, further normalized $P(i)$ to represent a Probability Density Function (PDF) of intensity level.

(ii) **Compute the CDF:**
The cumulative sum (cumulative distribution function) $C(i)$ of the normalized histogram is calculated using the cumulative probabilities of each intensity value. Computed for both the values below and above the threshold t:

- $\omega_b(t)$: Cumulative probability of pixels below threshold t (background).

$$\omega_b(t) = \sum_{i=0}^{t} P(i), \tag{4.2}$$

- $\omega_f(t)$: Cumulative probability of pixels above threshold t (foreground).

$$\omega_f(t) = 1 - \omega_b(t) \tag{4.3}$$

(iii) **Compute the Cumulative Mean:**
The cumulative mean up to each intensity level is calculated given:

- $\mu_b(t)$: Mean intensity of pixels below threshold t.

$$\mu_b(t) = \sum_{i=0}^{t} i \cdot \frac{P(i)}{\omega_b(t)}, \tag{4.4}$$

- $\mu_f(t)$: Mean intensity of pixels above threshold t.

$$\mu_f(t) = \sum_{i=t+1}^{255-1} i \cdot \frac{P(i)}{\omega_f(t)} \tag{4.5}$$

(iv) **Compute the Between-Class Variance:**
For each intensity level, the between-class variance $\sigma^2(t)$ is calculated to measure the separation between classes of pixels at that particular intensity level. Given by the

product of the square difference between the mean grayscale intensity values and the probabilities of the regions :

$$\sigma^2(t) = \omega_b(t) \cdot \omega_f(t) \cdot [\mu_b(t) - \mu_f(t)]^2 \tag{4.6}$$

(v) **Determine the Optimal Threshold:**
The threshold value that maximizes the between-class variance is chosen as the optimal threshold, which indicates the optimal separation between the foreground and the background.

$$T_{opt} = argmax(\sigma^2(t)) \tag{4.7}$$

Algorithm 4 Otsu's Method

Input: R ▷ ROI
Output: B ▷ Binary ROI, **B**
$H(R)$ ▷ Compute Histogram $H(R)$ of **R**
$P(R)$ ▷ Normalize Histogram $P(R)$
$C(R)$ ▷ Compute CDF $C(R)$
for T_0 to 255 **do**
    $\omega_b(t)$, $\omega_f(t)$ ▷ Compute region probabilities
    $\mu_b(t)$, $\mu_f(t)$ ▷ Compute region mean values
    $\sigma^2(t)$ ▷ Compute between-class variance
    T^* ▷ Select T^* that maximizes between-class variance;
end for
B←**applyThreshold**(**R**, T^*) ▷ Apply threshold T^* to **R**
return B ▷ Return Binary ROI

One of the advantages of the method its simplicity and speed in identifying the optimal threshold without needing previous information of the image to be processed, so for our application it is feasible to calculate the threshold in real-time.

It is worth mentioning that the method is designed to operate with grayscale images since it has a bimodal distribution, which matches our application. However, in cases with variable illumination, the segmentation of our object of interest can be challenging, potentially losing our object given the fluctuating intensities and not having a clear peak corresponding to our object.A situation similar to this is explained in Figure. 4.6, where we attempt to prevent with the enhancement of our image. Furthermore, applying the method through the ROI mechanism in a focused manner complements the effectiveness of Otsu's method streamlining the detection of the markers.

Kullback-Leibler Divergence Minimization

KL is a common loss function used in reinforcement learning and machine learning, measuring the difference between predicted and actual values. From a statistical perspective, it measures the difference between two probability distributions. In our specific context, we aim to utilize KL to determine the optimal threshold minimizing this criterion.

Given a set of random variables $X = \{x_1, \ldots, x_n\}$, where $x \in \{0, 1, \ldots, 255\}$ in our given problem defining the set of all pixel intensity values, and a pair of distributions, P_θ represents the reference probability distribution, and Q_ϕ represents the estimate distribution to be measured. The KL-divergence is formulated as follows:

$$D_{\mathrm{KL}}(P_\theta \| Q_\phi) = \sum_{x \in X} P_\theta(x) \log \left(\frac{P_\theta(x)}{Q_\phi(x)} \right) \tag{4.8}$$

KL has its origins in information theory and can be considered a slight modification of entropy that includes not only P_θ but Q_ϕ our approximated distribution.

$$Entropy : H(X) = -\sum_{x \in X} P(x) \log(P(x)) \tag{4.9}$$

Hence, KL divergence serves as a metric to measure the degree of information loss with our estimate distribution. In our specific scenario, the essence lies in binarizing the image while retaining its bright spots, resulting in distribution that closely resembles our initial ROI distribution, which supports determining the threshold with minimal information loss and potentially improving the relevance and accuracy of the segmentation.

Algorithm description

1. **Compute the reference distribution:**
   Histogram $H(i)$ of pixel intensities in the ROI is calculated, and then normalized $P(i)$ to represent the PDF of our reference distribution.
2. **Compute the estimate distribution**
   The PDF is calculated for a potential threshold t value given the reference distribution previously calculated, divided into two segments below and above t representing the background and foreground $Q_b(t)$ and $Q_f(t)$, respectively. Resulting in the estimate distribution for the potential t.
3. **Compute the KL divergence for segments**

   For the pair of segments that represent the estimate distribution, compute the KL divergence given the reference distribution to evaluate the overall divergence between our original ROI reference distribution.

$$D_{\mathrm{KL\ background}}(P \| Q_b(t)) = \sum_{i=0}^{n} P(i) \log \left(\frac{P(i)}{Q_b(i)} \right) \tag{4.10}$$

$$D_{\mathrm{KL\ foreground}}(P \| Q_f(t)) = \sum_{i=0}^{n} P(i) \log \left(\frac{P(i)}{Q_f(i)} \right) \tag{4.11}$$

$$D_{\mathrm{KL\ total}}(t) = D_{\mathrm{KL\ background}} + D_{\mathrm{KL\ foreground}} \tag{4.12}$$

4. **Determine the Optimal Threshold:**
   The threshold value that minimizes the KL Divergence is chosen as the optimal threshold, which indicates the binarized distribution that most closely resembles our reference ROI distribution.

$$T^* = argmminD_{KLtotal} \tag{4.13}$$

Algorithm 5 KL Divergence Minimization

Input: R ▷ ROI
Output: B ▷ Binary ROI, **B**
$H(R)$ ▷ Compute Histogram $H(R)$ of **R**
$P(R)$ ▷ Normalize Histogram $P(R)$
for T_0 to 255 **do**
    $Q_b(T))$, $Q_f(T))$ ▷ Compute estimate distribution segments
    $D_{\text{KL background}}$, $D_{\text{KL foreground}}$ ▷ Compute the KL divergence for segments
    $D_{\text{KL total}}(t) = D_{\text{KL background}} + D_{\text{KL foreground}}$ ▷ Get total KL divergence
    T^* ▷Find T^* that minimize KL divergence
end for
B←**applyThreshold**(**R**, T^*) ▷ Apply threshold T^* to **R**
return B ▷ Return Binary ROI

By minimizing $D_{\text{KL total}}(t)$, the goal is to find a threshold that makes the segmented distributions as similar as possible to the respective ROI reference distribution, thereby minimizing information loss and potentially improving the relevance and accuracy of the segmentation. Finding the threshold that minimizes loss of information for our communication problem can be a valuable method, using our original signal to preserve the LED characteristics.

Compared to Otsu's Method, it represents a suitable alternative because uneven light conditions can lead to unsatisfactory results if we are seeking only the best separation. A good comparison is demonstrated in Figure. 4.10 the results with the Otsu's method with an area corresponding to the background exhibit an incorrectly segmented background area, whereas in KL method only the high-frequency components remain.

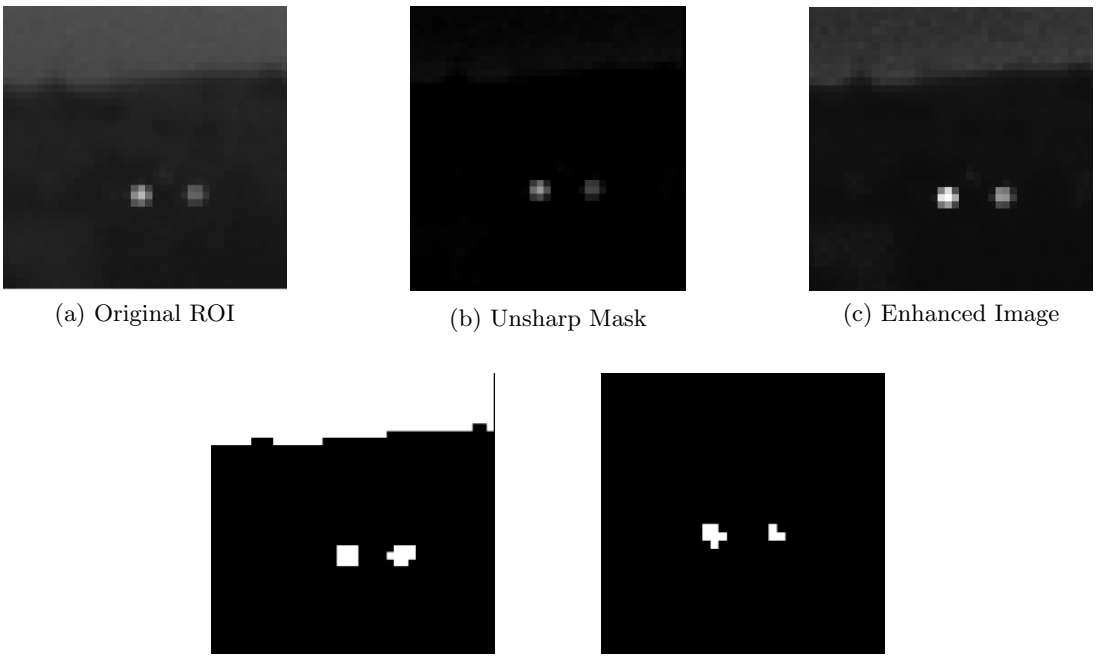

(a) Original ROI (b) Unsharp Mask (c) Enhanced Image

(d) Binary ROI with Otsu's method (e) Binary ROI with KL method

Figure 4.10: Comparison of adaptive thresholding methods.

- **Merging of detected points**

One of the last steps before providing the position of the candidate points in the image is evaluating the points obtained by the adaptive process and comparing them with those initially obtained through static binarization. Although we retain the initial detections, we have priority when our method provides results in their region. The main objective of this process is to include in its result those points out of range of the ROI areas that are potentially coming from UAVs not initially present in the LoS concerning the UAV RX. With this process, in cases where a UAV enters the LoS later in the operation, it will be considered and delivered to the next module of the system, being received in the feedback in a later stage for being processed adaptively with its corresponding ROI.

5 Performance Evaluation

Contents

For validation of the proposed adaptive algorithm, simulation, and field experiments were designed and executed for its evaluation. The motivation of the algorithm is to be compatible with the current system and to achieve similar or better results with the current static threshold implementation.

The design of the experiments takes into account the limitations, variations of pixel intensity due to distance and orientation, presented in Chapter 3. Therefore, the objective of the evaluation of the experiments is to compare the performance at different operating distances and particular orientations to evaluate and compare the proposed method with the static method to confirm the limitations presented.

The MRS system [17], which integrates UVDAR operation tools, was used to validate the simulator in the Gazebo. A significant factor for evaluating the algorithm, in terms of vision, the simulator is insufficient for the detailed validation of our adaptive methods because the background in the image remains static with a simplified gray background, this is due to the simulated image stream being simplified for performance reasons. Nevertheless, the optical and lambertian radiation properties are included in the LEDs, functioning as a development tool to validate compatibility with the system. The recordings from the desert experiments were also helpful in testing the performance by having recordings of real-world experiments for running the UVDAR locally to evaluate the segmentation results.

5.1 Simulation and testing

The simulator helped to design the experiments and to validate the findings before the real-world experiments. We set up 1 RX and 1 TX to evaluate the performance with increasing distance, being able to conduct various experiments and gathering results searching for insights for evaluation in the real world.

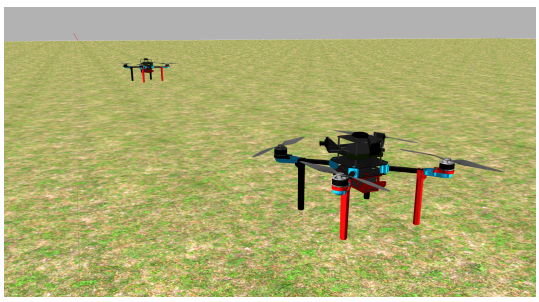

(a) RX and TX at 5m.

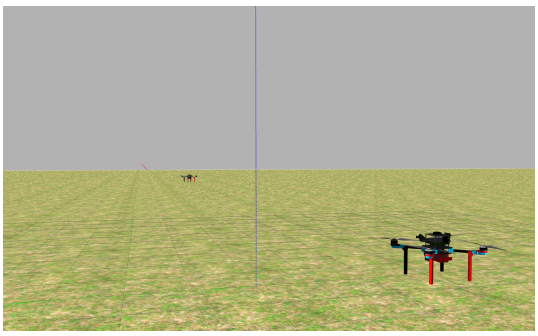

(b) RX and TX at 15m.

Figure 5.1: Gazebo simulator experiments.

Increasing distance evaluation

For this purpose, we collect data from the tracking output to evaluate the decoding of the TX signals and to compare our adaptive approach with Otsu's method and KL divergence against the SOTA detection algorithm using the static threshold, testing it with different thresholds to independently assess the threshold impact on the communication range. To evaluate the difference between the results with UAV in motion and stationary, we collected data every 2 meters of the identified sequence from the output of the blink processor module, obtaining data from stationary conditions, These results are presented in Figure 5.2 with the "static" label. The data labeled "dynamic" indicates the measurements included the movements transitioning to each distance.

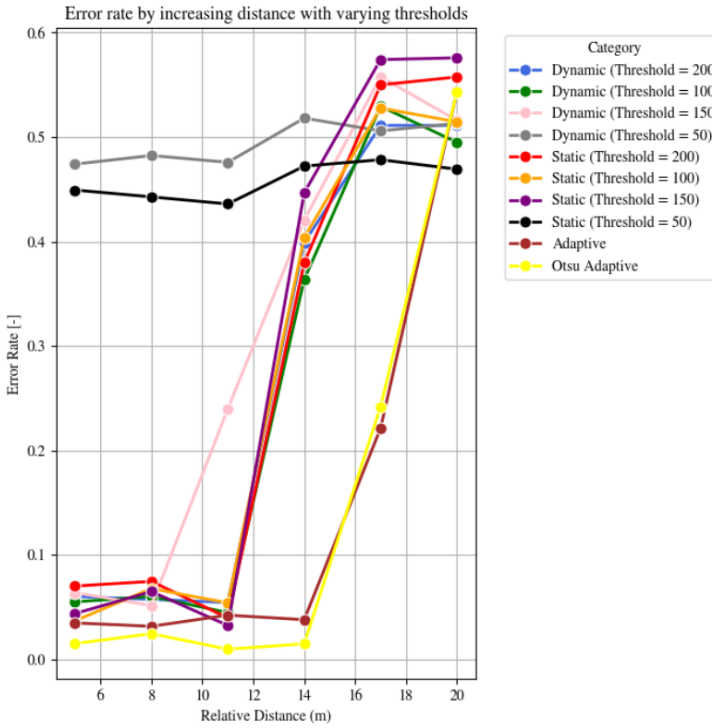

Figure 5.2: Simulation: Error rate comparison with respect to increasing distance for SOTA and adaptive methods.

When comparing the methods, we observe that with the static method, the error rate remains low until the distance of 11m, starts to rise at 12m with an error rate between 40 and 50%, whereas with our adaptive approach, we achieve minimal error rate until 14m and it start to increase at a distance of 16m with an error rate of 20%.

This represents a considerable improvement and demonstrates the potential of the algorithm. In terms of detection and vision, the simulator is not challenging for our problem as it does not present a challenge for segmentation. However, an improvement in the simulator presents the potential of the approach, with more accurate processing by performing the segmentation in a localized way with the ROI mechanism, performing a more accurate point separation and contours not fading in the background as in the real world, while the SOTA algorithm that uses circular neighborhood separation can be merging close points that complicates the decoding.

Although the background does not present a challenge for the segmentation, we were

able to validate the threshold detection deficiencies. For high values, comparable results were obtained, with the effect of a low threshold showing that it is more permissive to the background adding complexity to the LED detection represented by a higher error rate.

- **Challenging heading**

The second validation performed was to change the relative orientation of the TX to have a challenging orientation in terms of detection by having LEDs close to each other, causing interference with increasing distance.

Obtaining better decoding results as the distance increases indicates the adaptive algorithm has higher accuracy than the static implementation, illustrated in Figure 5.5. In the static implementation, the accuracy may have been affected by the the neighborhood separation, which would explain the difference in performance in the simulator.

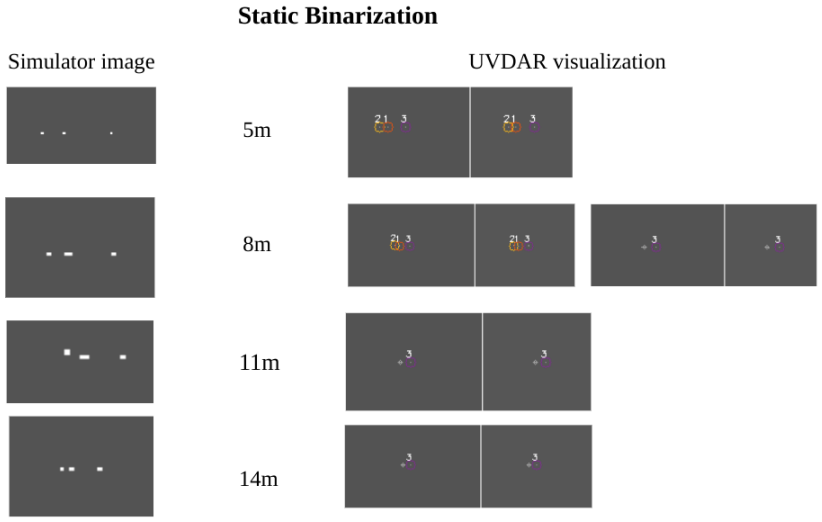

Figure 5.3: Simulator comparison of Signal 1 and 2 presence through increasing distance

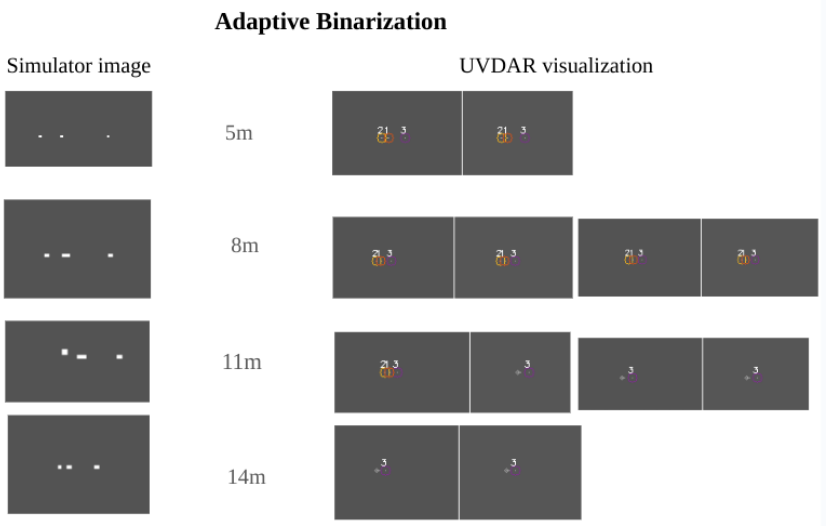

Figure 5.4: Simulator camera view of Signal "1" and "2" decoding with increasing distance

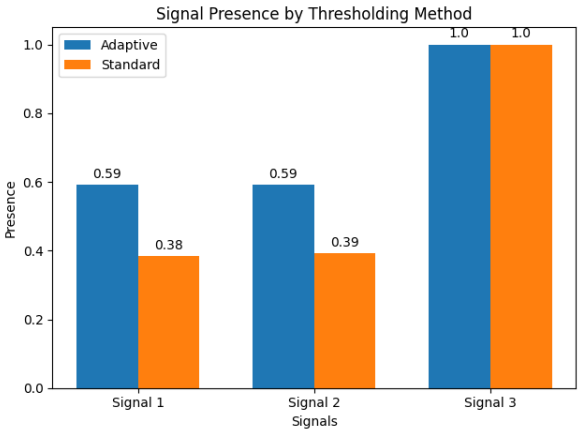

Figure 5.5: Simulator camera view of Signal "1" and "2" decoding with increasing distance for Otsu's method and SOTA.

5.2 Real-world Application and Results

Maximal LED Separation (Exposure 1000us)

The objective of the firs experiment was to assess the effectiveness of communication and detection. Therefore, using 1 RX and 1 TX emitting the signals with $ID = \{0, 1, 3\}$, initially both with a relative distance of 5 meters, having one camera of the receiver pointing directly to the TX. The TX increases its distance w.r.t RX for evaluating the operational distance performance. The TX relative orientation was chosen to have the maximum separation of the LEDs as explained in Figure. 5.9.

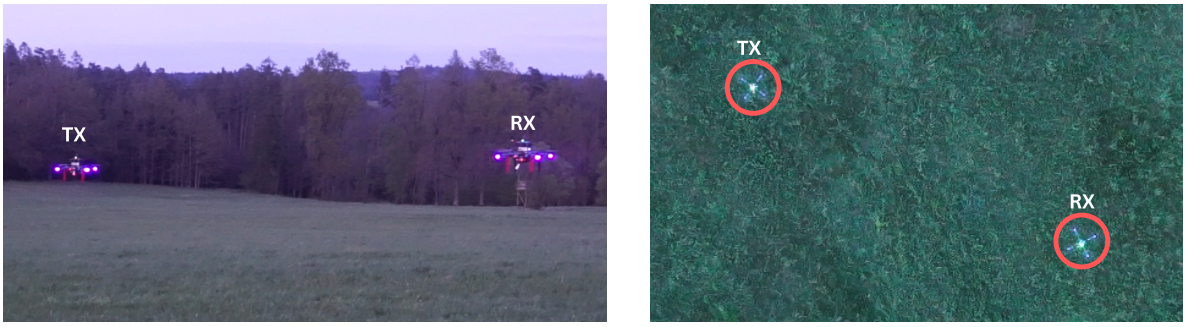

Figure 5.6: (a) Front view of the initial experiments setup at 5 meters. (b) Aerial View.

The MRS system [17] was used in the creation of the experiments, and both UAVs were equipped with Real-Time Kinematic (RTK) receiver for corrections with GNSS system to guarantee precise positioning. The sequences extracted from the the tracking module were used for evaluation as a basis for a performance metric. The TX trajectory, starting 5 meters w.r.t RX, increasing its distance by 5 meters every 30 seconds until reaching a relative distance of 30 meters.

In this first set of experiments, we obtained a similar performance in terms of error rate for the static and adaptive methods; as seen in previous results discussed in Chapter 3, having an increase in the error rate at 15 meters . With significant improvement of 24% lower at 20

meters and 7 % with the adaptive methods of Otsu's method and KL Divergence, respectively than the SOTA while increasing distance.

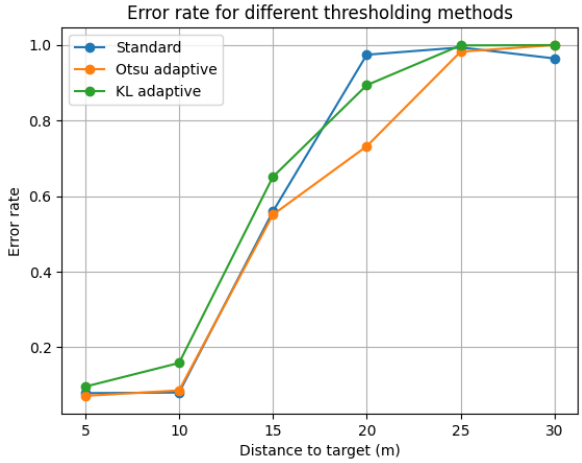

Figure 5.7: Error rate with respect to increasing distance for SOTA and adaptive methods. (1000 us).

Significant to note that ambient noise from bright spots from sources other than LED may bias the error rate. Therefore, the decoding of the signals selected for the TX LEDs through increasing distance was evaluated.

Table 5.1: Overall presence per signal comparison (Exposure 1000us)

Signal	Otsu Adaptive Method	Standard Method	KL Adaptive Method
0	0.583640	0.345191	0.494267
1	0.349622	0.387539	0.309517
3	0.346090	0.418324	0.389494

On average, the adaptive methods have a higher signal decoding than the static methods. Otsu's method has a higher decoding overrall of 58%, KL Divergence approximately 49%, and 34% with the SOTA method. The drops, illustrated in Figure. 5.8, observed at each interval of distance represent the points where the TX was moving towards its next distance until the signal is recovered while being stationary. Interestingly, signals 1 and 3 had a similar decoding success.

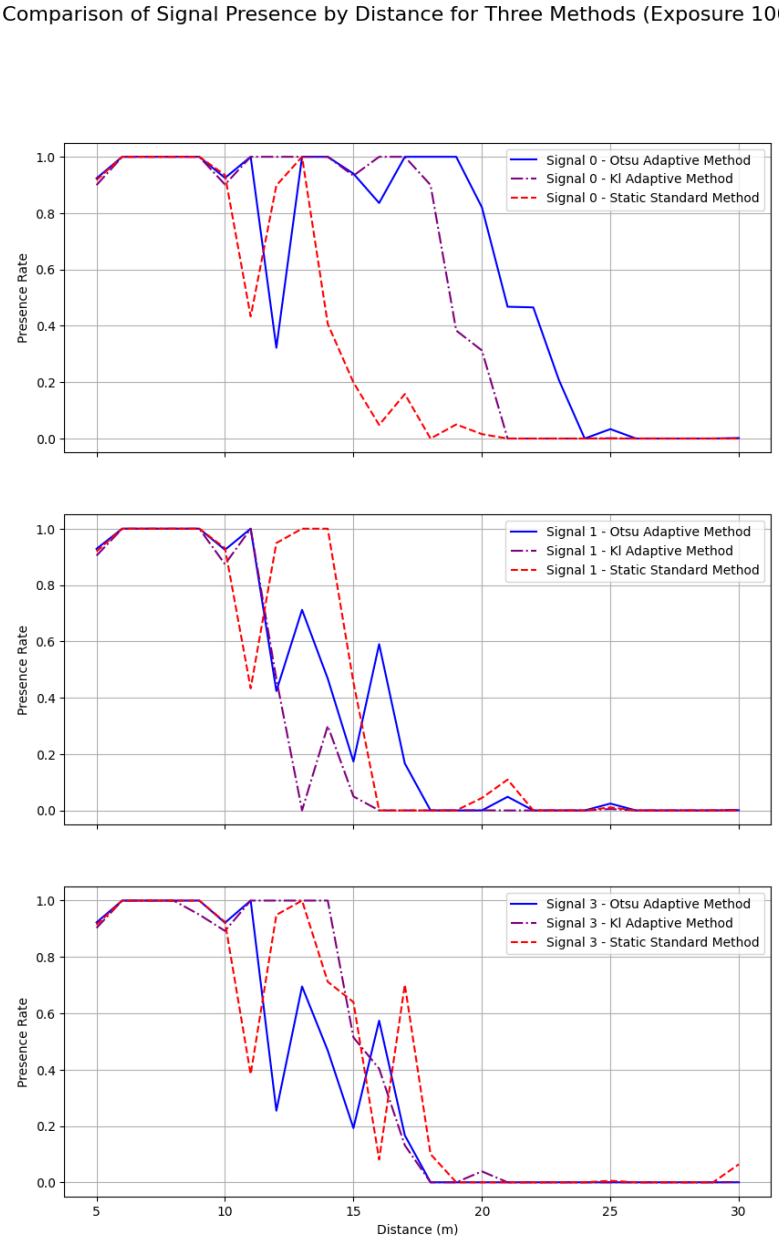

Figure 5.8: Signal presence rate comparison with respect to increasing distance for SOTA and adaptive methods. (Exposure 1000us)

On further visual investigation of the image, we found that at the start of the experiment the separation of the LEDs was not as ideal with LEDs close to other (seen in Figure. 5.9). This because magnetometer estimation for the heading is not accurate, For an accurate heading estimation a dual RTK setup would be necessary to calculate the heading based on the relative position of the antennas equipped in the UAV. Nonetheless, the ”0” signal that did not suffer any interference from the other LEDs served as a reference to demonstrate the performance and to compare the methods.

However, it would not be fair to evaluate only the success of the communication since it does not depend only on our algorithm for decoding the signals but also on the capacity of

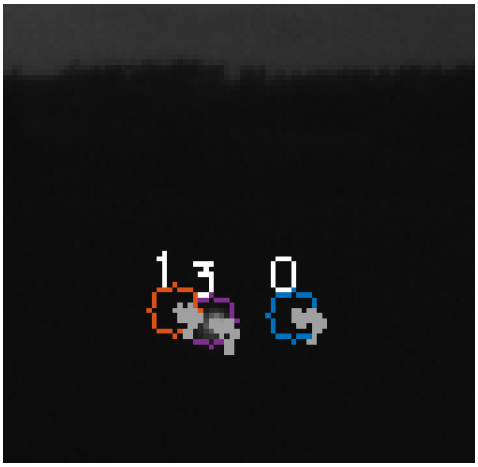

Figure 5.9: Signal ID vizualization from Otsu's method experiment (1000us).

the tracking algorithm.

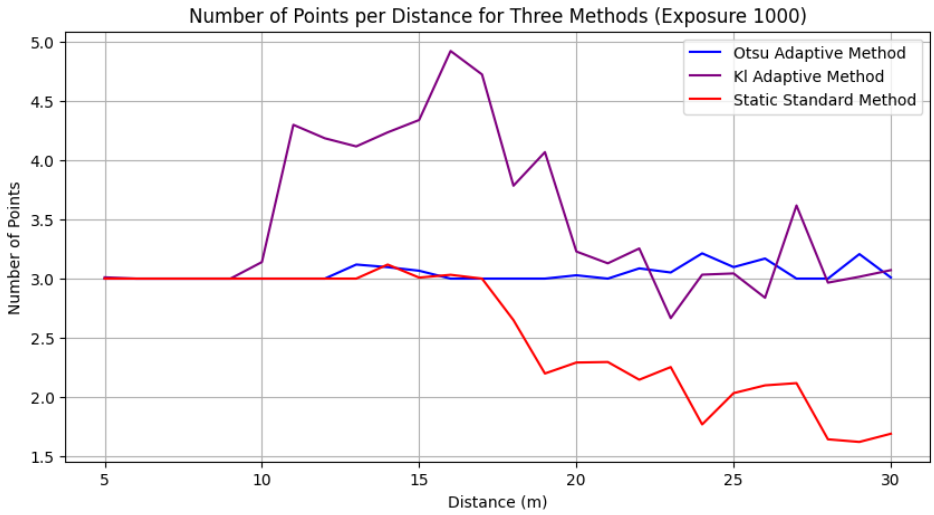

Figure 5.10: Overall number of detected with respect to increasing distance for SOTA and adaptive methods. (1000 us).

Analyzing the detection performance, we found that the static method decreases the number of detections around 17 meters, while the adaptive methods maintain obtaining the three LEDs' along the 30-meter trajectory; this could be a factor that explains the previously observed limitation of 15m operating range, affected by the static threshold limit in the SOTA algorithm. Otsu's method achieves a stable detection of the LEDs from 20 meters, which implies that the detection as such exhibits a significant improvement compared to the SOTA method.

The reason why the LEDs are successfully detected but the tracking fails to correctly decode them would necessitate further investigation. A possible reason is that the points provided are not in a suitable frequency than our expected signal, implying further optimization is needed to accurately provide these small dots in the image over long distances.

It should be noted that KL method retrieved a higher number of points, which is under-

standable given that it would be more likely to preserve background details, as it minimizes the divergence with the original ROI, confirming that it is more likely to introduce noise. However, the signal decoding performance was similar to Otsu's method for a distance up to 20 meters, as seen in Figure 5.8.

- **Maximal LED Separation (Exposure 500us)**

The second set of experiments consisted of repeating the same methodology as the first experiment set, With the distinction that the exposure time was decreased to 500 us evaluate if the performance improved, as the image would become darker. Compared to the SOTA implementation using static threshold illustrated in Figure 5.11, Otsu's method produced a 35% lower error rate at a distance of 15 meters.

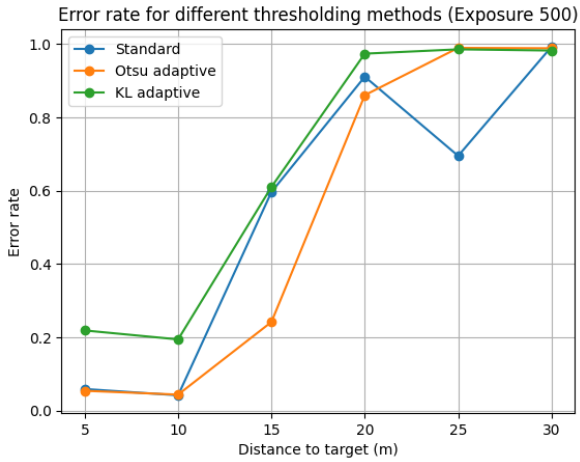

Figure 5.11: (a) Error rate with respect to increasing distance for SOTA and adaptive methods. (500 us).

Table 5.2: Overall Presence per signal comparison (Exposure 500us)

Signal	Otsu Adaptive Method	Standard Method	KL Adaptive Method
0	0.480427	0.414743	0.415961
1	0.428155	0.380285	0.351910
3	0.501919	0.555994	0.489435

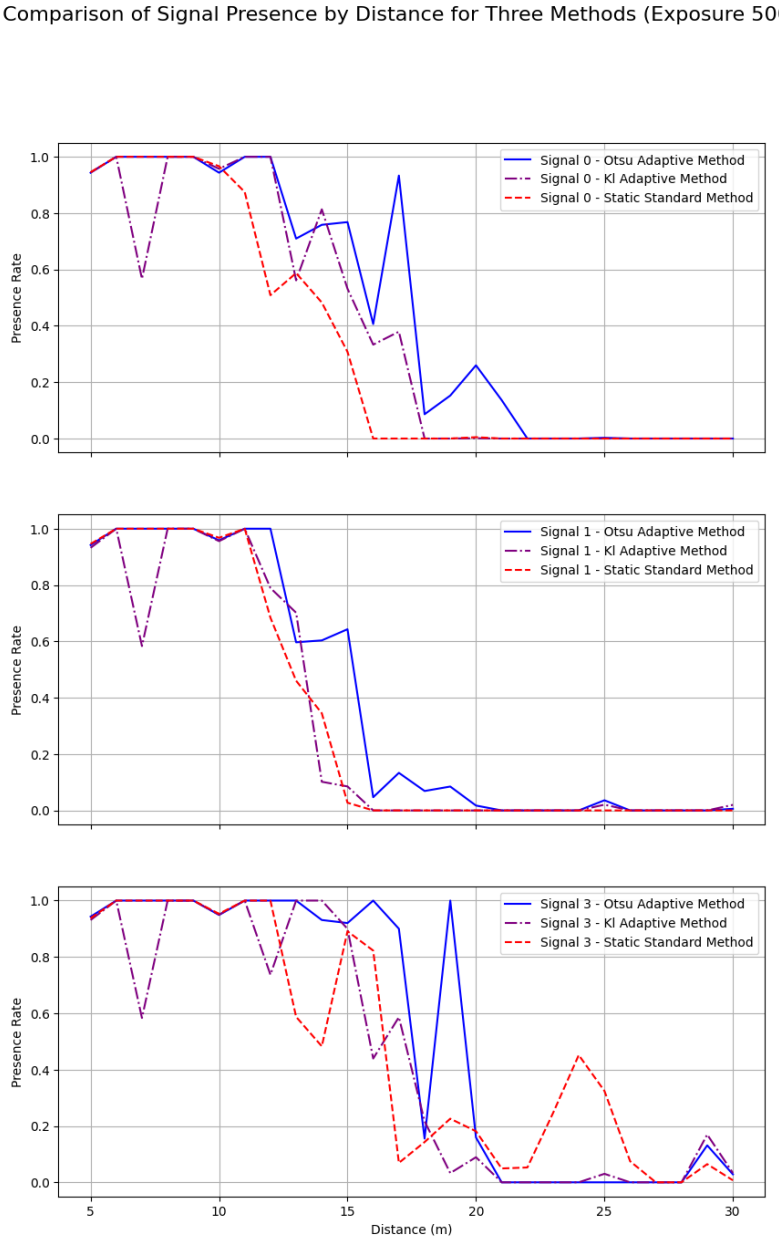

Figure 5.12: Comparison of signal decoding rate with respect to increasing distance for SOTA and adaptive methods. (Exposure 500us)

By reducing the exposure, we naturally increase the accuracy by achieving a lower error rate with the Otsu method and even a slightly higher decoding with the SOTA method with static thresholding. However, the operation range is reduced to around 5 meters for the SOTA, as from 10 meters beyond, the decoding of signal begins to decrease.

This happens for the adaptive methods as well, reducing the operational distance in comparison to the 1000 exposure results but still surpassing the SOTA method, as we can observe the offsets in Figure. 5.12 , the decrease for the adaptive methods happens at a further distance, with the best performance in Otsu's method maintaining around 17 meters the signal decoding above 80% for signals "0" and "3", as seen in Figure 5.12. Signal "3" interfering

being above LED with Signal "1", making it difficult to decode the other. This explains the decrease of succesfull decoding for Signal "1", having only one of the LEDs decoded correctly.

As a result of the observations that greater precision is achieved with reduced exposures, performance optimization strategies emerge. Previously, the range of operation was the major limitation for the static approach because of the smaller size and intensity of bright spots detected with lower exposure. Now that we employ the adaptive thresholding, we can operate with lower exposure time. This provides the opportunity to find a configuration that optimizes the adaptive method while preserving the desired operating range.

As for the detected points, the decline in the number of the detected points at closer distances for the SOTA method, as illustrated in Figure 5.13. However, the adaptive methods number of detections continue over 30 meters, where a change in the stability of the points was observed a few meters earlier for Otsu's method. For KL Divergence method, compared with the higher exposure, the number of defections was also lower. As before more than three points where detected along the experiment, which could be from segmented points from background, introduced as noise given the minimization is over fitting the original ROI.

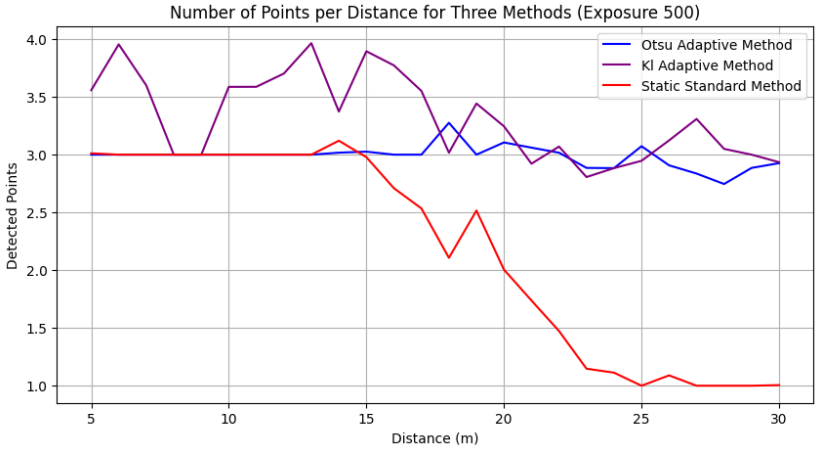

Figure 5.13: Overall number of detected with respect to increasing distance for SOTA and adaptive methods. (500 us).

Challenging Heading

To assess the scenario described in Chapter 3, illustrated in Figure. 3.8 with LEDs close to another in the image with certain headings w.r.t RX, the final set of experiments uses a heading where this scenario happens to evaluate as the distance between the RX and TX increases the effect in the decoding. The static method seems to have a lower error rate than the adaptive methods at the first distance of 5m (Figure. 5.14). However, it is difficult to effectively compare the methods given the lack of precision necessary for duplicating the same heading. For instance, with Otsu's method in the initial distance of 5m the LEDs "1" and "3" interfere with each other, illustrated in Figure. 5.15.

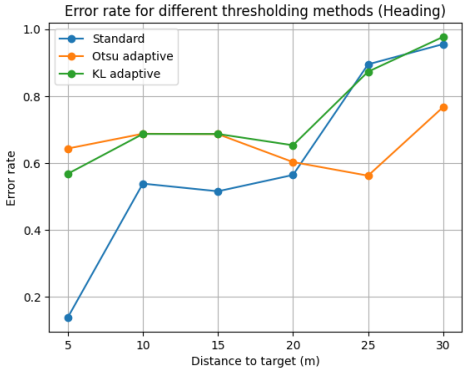

Figure 5.14: (a) Heading experiment: Error rate with respect to increasing distance (1000 us).

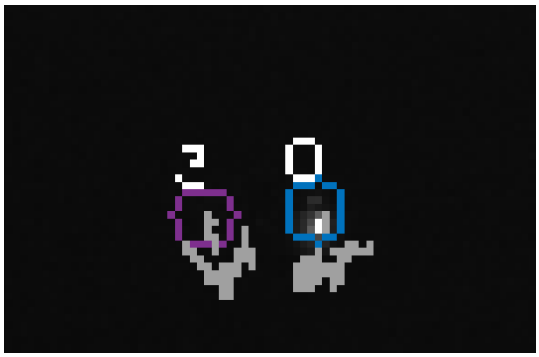

(a) Signal "0" and "3" are present, missing Signal "1"

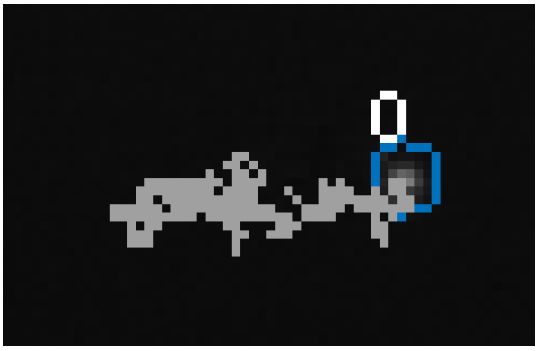

(b) Pixel interference causing a failure in decoding

Figure 5.15: Otsu signal ID's at 5m.

However, when analyzing the detected points over distance, there is a significant difference between the static and adaptive methods, as shown in Figure. 5.16. Initially, the static method detects all 3 LEDs, with a low error rate. However, when transitioning to 10 meters, the detection of the points decline, only detecting two points, confirming the disadvantage of the SOTA method with neighborhood separation mentioned in Chapter 3, even though the points does not converge they are detected as a single marker. Effect that does not occur for the adaptive methods, detecting three points up to 15 meters. Further from 15 meters the stability of the points detected decreases, which may explain the points being successfully extracted less frequently.

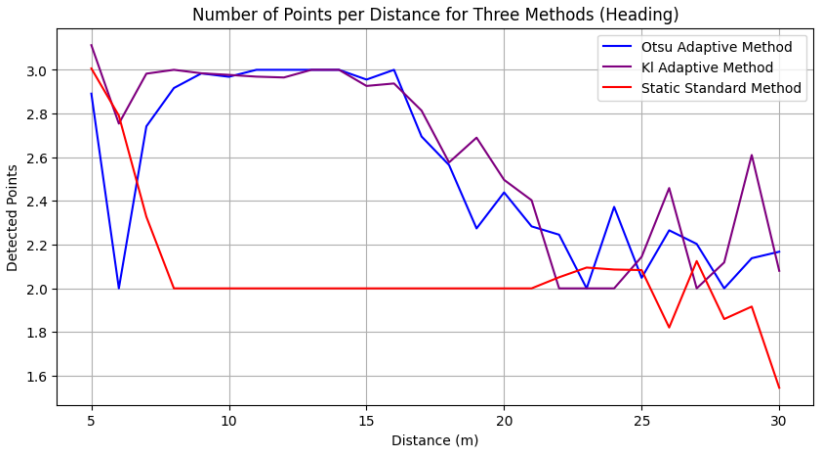

Figure 5.16: Heading experiment: Overall number of detected points with respect to increasing distance (1000us).

However, in Figure. 5.16, at a distance of approximately 20 meters indicates where the points converge, resulting in the detection of only two points. Although the decoding of the signal was not successful, it demonstrates the potential and higher detection accuracy of the adaptive methods compared with the SOTA using static thresholding. Further efforts would be needed to solve the issue of pixel interference.

As shown in the Figure. 5.17, Signals ”1” and ”3” had a low decoding when keeping this challenging orientation, demonstrating the importance of orientation.

5.3 Evaluation

The results obtained from the experiments effectively compared the SOTA method using static threshold approach with the adaptive thresholding methods. In terms of distance, the adaptive methods had a higher signal decoding rate. However, in the heading experiments the SOTA method achieved lower error rates. An explanation could be the inability to replicate the same heading conditions for the set of experiments, where would be needed to compare them using the same dataset.

There is a chance that pixel interference will affect the adaptive centroid calculation during the CCA process if points that are close to each other connect, which would reflect the decoding error, additional investigation is required to validate this hypothesis, in addition to implementing erosion techniques to prevent such occurrences.

In terms of detection, there is a significant difference, detecting the LED continuously along the 30 meters, demonstrating the potential and opportunity of the proposed solution. Comparing the adaptive methods applied, Otsu’s method outperformed KL Divergence minimization and the SOTA method in terms of decoding and detection. KL achieved a higher decoding rate than the static method, but introduced more noise in the segmentation process.

Finally, the results demonstrate we can achieve lower error rates by reducing exposure at the cost of decreasing the operating range, with the adaptive methods having a smaller impact on the communication range compared to the static method.

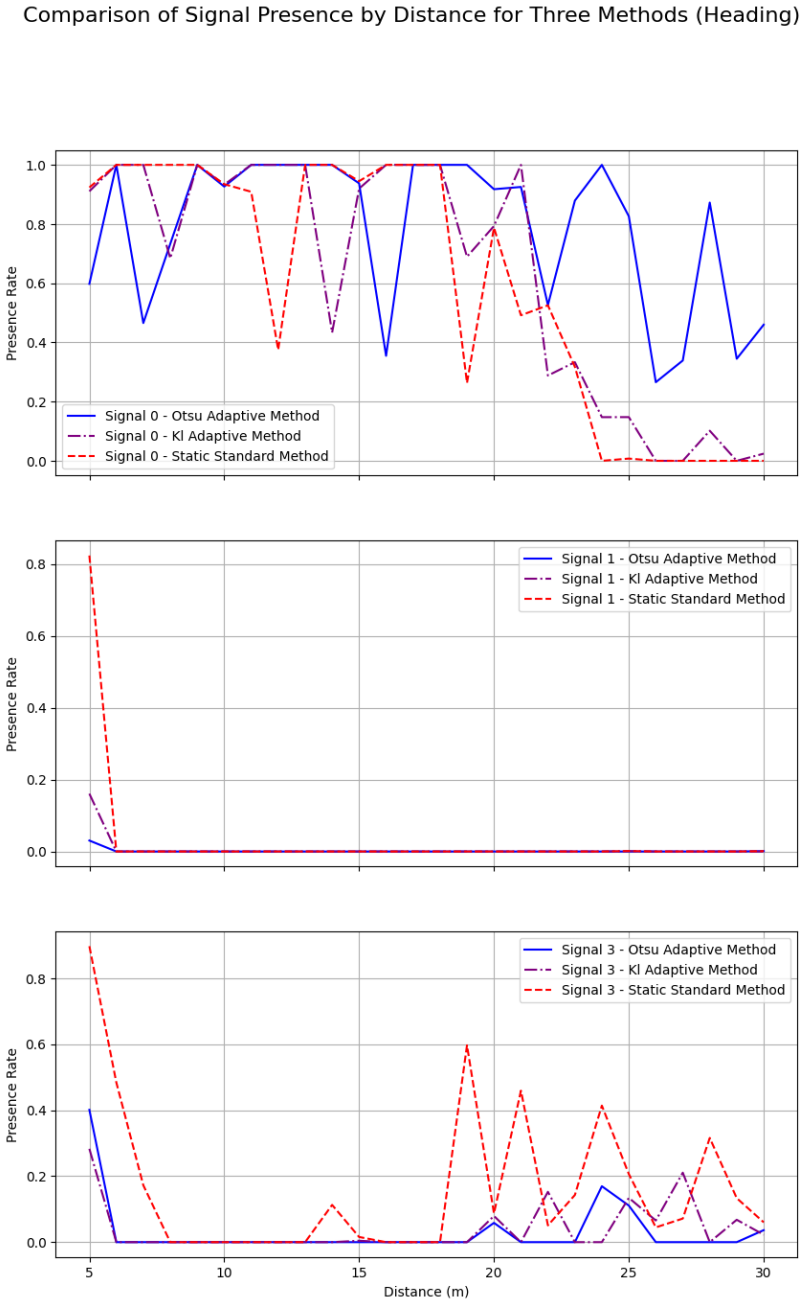

Figure 5.17: Heading experiment: Comparison of signal decoding rate with respect to increasing distance for SOTA and adaptive methods (1000us).

6 Conclusion

This thesis aimed to develop an adaptive thresholding algorithm to enable the detection of UV-LEDs in the UVDAR System. The study investigated the constraints of the current state-of-the-art approach, supported by analyzing data from previous experiments.

An ROI approach was proposed, performing local processing utilizing the tracking algorithm as feedback. The ROI processing strategies ensure effective segmentation to provide the location of the UV LEDs to the rest of the system.

The motivation for the ROI approach was inspired by multi-robot operation, allowing it to adapt to process multiple UAVs locally independently to improve the decoding accuracy of each signal present. The method was incorporated into the UVDAR system, and tested with different experiments in the Gazebo simulator. Furthermore, several real-world experiments were conducted.

All of the following tasks have been completed in accordance with the thesis requirement:

(i) The state-of-the-art from OCC was studied and current limitations for integration with UAVs were discussed in Chapters 1 and 2.
(ii) The UVDAR system was studied and the limitations were discussed in Chapter 3.
(iii) The data from previous experiments was extracted and analyzed characterizing the distributions of the pixel intensities of UV LEDs in Chapter 3.
(iv) The design of the adaptive algorithm is described in Chapter 4 and compared with the static method in Chapter 5.
(v) The system was verified through the simulation environment, and real-world experiments were conducted to evaluate the performance regarding error rate with increasing distance compared with the static method in Chapter 5.

6.1 Future work

Based on the results presented, it will be necessary to investigate further scenarios of pixel interference. Therefore, a dual-RTK setup will be necessary for accurately replicating the orientations and comparing the performance.

As for the development of the algorithm, there is room for improvement since new adaptive thresholding techniques can be developed and tested in the algorithm, being simple to switch the adaptive technique in the ROI algorithm.

It will also be necessary to analyze in more detail the decoding at long distances because it showed better detection of the LEDs but the signal was not successfully detected, so it may be necessary to optimize the detection process for long distances.

Additionally, to perform further experiments for comparison with multiple UAVs to evaluate the difference of having multiple TX with different distances, as this is one of the motivations and strengths of the adaptive algorithm.

Finally, we primarily concentrated on assessing the performance of communication; however, it would be valuable to consider evaluating the performance of localization as well, given that the small ROI approach enhances detection and could also have lower pose uncertainty.

7 References

[1] T. Lakemann, *Ami - anonymous blinking marker tracking*, GitHub repository, 2024. [Online]. Available: https://github.com/TimLakemann/ami.

[2] Y.-H. Chang, D.-C. Tsai, C.-W. Chow, *et al.*, "Lightweight light-diffusing fiber transmitter equipped unmanned-aerial-vehicle (uav) for large field-of-view (fov) optical wireless communication," in *2023 Optical Fiber Communications Conference and Exhibition (OFC)*, 2023, pp. 1–3. DOI: 10.1364/OFC.2023.Th3H.6.

[3] J. Horyna, T. Baca, V. Walter, and et al., "Decentralized swarms of unmanned aerial vehicles for search and rescue operations without explicit communication," *Autonomous Robots*, vol. 47, pp. 77–93, 2023. DOI: 10.1007/s10514-022-10066-5. [Online]. Available: https://doi.org/10.1007/s10514-022-10066-5.

[4] D. B. Licea, V. Walter, M. Ghogho, and M. Saska, *Optical communication-based identification for multi-uav systems: Theory and practice*, 2023. arXiv: 2302.04770 [eess.SP].

[5] V. Vrba, "Implementation of image processing in the uvdar system on fpga," Master's thesis, Czech Technical University in Prague, Faculty of Electrical Engineering, Department of Cybernetics, Prague, Czech Republic, 2023. [Online]. Available: https://dspace.cvut.cz/handle/10467/107170.

[6] X. Zhang, G. Klevering, X. Lei, Y. Hu, L. Xiao, and G.-H. Tu, "The security in optical wireless communication: A survey," *ACM Computing Surveys*, vol. 55, pp. 1 –36, 2023. DOI: 10.1145/3594718.

[7] X. Zhang, G. Klevering, J. Mariani, L. Xiao, and M. Mutka, "Boosting optical camera communication via 2d rolling blocks," *2023 IEEE/ACM 31st International Symposium on Quality of Service (IWQoS)*, pp. 1–4, 2023. DOI: 10.1109/IWQoS57198.2023.10188746.

[8] A. Ahmad, D. Bonilla Licea, G. Silano, T. Baca, and M. Saska, "PACNav: A Collective Navigation Approach for UAV Swarms Deprived of Communication and External Localization," *Bioinspiration Biomimetics*, vol. 17, pp. 1–19, 6 2022, ISSN: 1748-3190. DOI: 10.1088/1748-3190/ac98e6. [Online]. Available: https://iopscience.iop.org/article/10.1088/1748-3190/ac98e6.

[9] M. Alp Merzi, V. Gazi, G. Fedele, L. D'Alfonso, and A. Bono, "Target capturing in an ellipsoidal region with a swarm of quadrotor uavs," in *2022 International Conference on Unmanned Aircraft Systems (ICUAS)*, 2022, pp. 972–981. DOI: 10.1109/ICUAS54217.2022.9836166.

[10] G. Chen, T. Wu, F. Yang, T. Wang, J. Song, and Z. Han, "Ultraviolet-based uav swarm communications: Potentials and challenges," *IEEE Wireless Communications*, vol. 29, no. 5, pp. 84–90, 2022. DOI: 10.1109/MWC.007.2100405.

[11] J. Horyna, V. Walter, and M. Saska, "UVDAR-COM: UV-Based Relative Localization of UAVs with Integrated Optical Communication," in *2022 International Conference on Unmanned Aircraft Systems (ICUAS)*, IEEE, 2022. DOI: 10.1109/ICUAS54217.2022.9836151.

[12] Y. Onodera, Y. Nakayama, H. Takano, and D. Hisano, "Drone positioning for visible light communication with drone-mounted led and camera," in *2022 IEEE 19th Annual Consumer Communications Networking Conference (CCNC)*, 2022, pp. 357–362. DOI: 10.1109/CCNC49033.2022.9700576.

[13] X. Sun, Y. Yu, and Q. Cheng, "Led recognition method based on deep learning in uav optical camera communication.," *Applied optics*, vol. 61 29, pp. 8688–8694, 2022. [Online]. Available: https://api.semanticscholar.org/CorpusID:252026531.

[14] H. Takano, M. Nakahara, K. Suzuoki, Y. Nakayama, and D. Hisano, "300-meter long-range optical camera communication on rgb-led-equipped drone and object-detecting camera," *IEEE Access*, vol. 10, pp. 55 073–55 080, 2022. DOI: 10.1109/ACCESS.2022.3177140.

[15] A. Ahmad, V. Walter, P. Petracek, *et al.*, "Autonomous Aerial Swarming in GNSS-denied Environments with High Obstacle Density," in *2021 IEEE International Conference on Robotics and Automation (ICRA)*, IEEE, 2021, pp. 570–576. DOI: 10.1109/ICRA48506.2021.9561284.

[16] T. Amorim, T. Nascimento, P. Petracek, G. de Masi, E. Ferrante, and M. Saska, "Self-organized uav flocking based on proximal control," in *2021 International Conference on Unmanned Aircraft Systems (ICUAS)*, 2021, pp. 1374–1382. DOI: 10.1109/ICUAS51884.2021.9476847.

[17] T. Baca, M. Petrlik, M. Vrba, *et al.*, "The MRS UAV System: Pushing the Frontiers of Reproducible Research, Real-world Deployment, and Education with Autonomous Unmanned Aerial Vehicles," *Journal of Intelligent & Robotic Systems*, vol. 102, no. 26, pp. 1–28, 1 May 2021.

[18] A. Dmytruk, T. Nascimento, A. Ahmad, T. Báča, and M. Saska, "Safe tightly-constrained uav swarming in gnss-denied environments," in *2021 International Conference on Unmanned Aircraft Systems (ICUAS)*, 2021, pp. 1391–1399. DOI: 10.1109/ICUAS51884.2021.9476794.

[19] N. S. Kordavani, A. Gholami, E. Hamidnejad, N. M. Esfahani, and Z. Ghassemlooy, "Experimental investigation of an adaptive v2v optical camera communications system," *2021 17th International Symposium on Wireless Communication Systems (ISWCS)*, pp. 1–5, 2021. [Online]. Available: https://api.semanticscholar.org/CorpusID:238994293.

[20] F. Norouzi, S. Olyaee, and M. M. Rad, "Bit error rate improvement in optical camera communication based on rgb led," *2021 29th Iranian Conference on Electrical Engineering (ICEE)*, pp. 47–50, 2021. DOI: 10.1109/ICEE52715.2021.9544287.

[21] Y. Onodera, Y. Nakayama, H. Takano, and D. Hisano, "Avoiding inter-light sources interference in optical camera communication," *2021 IEEE Global Communications Conference (GLOBECOM)*, pp. 1–6, 2021. DOI: 10.1109/GLOBECOM46510.2021.9685373.

[22] M. E. Plissiti, C. Papaioannou, Y. Sfikas, *et al.*, "An efficient adaptive thresholding scheme for signal decoding in nlos vlc systems," in *2021 IEEE International Mediterranean Conference on Communications and Networking (MeditCom)*, 2021, pp. 378–382. DOI: 10.1109/MeditCom49071.2021.9647560.

[23] M. H. Rahman, M. Shahjalal, M. K. Hasan, M. O. Ali, and Y. M. Jang, "Design of an svm classifier assisted intelligent receiver for reliable optical camera communication," *Sensors (Basel)*, vol. 21, no. 13, p. 4283, Jun. 2021. DOI: 10.3390/s21134283.

[24] H. Takano, D. Hisano, M. Nakahara, *et al.*, "Visible light communication on led-equipped drone and object-detecting camera for post-disaster monitoring," in *2021 IEEE 93rd Vehicular Technology Conference (VTC2021-Spring)*, 2021, pp. 1–5.

[25] Y. Noma and W. Chujo, "Line-of-sight distance extension of rolling-shutter occ using dual-camera spatial luminance distribution," *2020 IEEE Globecom Workshops (GC Wkshps*, pp. 1–6, 2020. DOI: 10.1109/GCWkshps50303.2020.9367431.

[26] S. R. Teli, V. Matus, S. Zvanovec, R. Perez-Jimenez, S. Vitek, and Z. Ghassemlooy, "Optical camera communications for iot–rolling-shutter based mimo scheme with grouped led array transmitter," *Sensors*, vol. 20, no. 12, 2020, ISSN: 1424-8220. DOI: 10.3390/s20123361. [Online]. Available: https://www.mdpi.com/1424-8220/20/12/3361.

[27] T. Tripp, A. S. Hamza, B. Underwood, and R. Tashakkori, "Low-cost ufsook-based optical camera communication link for iot applications," *2020 IEEE 6th World Forum on Internet of Things (WF-IoT)*, pp. 1–6, 2020. DOI: 10.1109/WF-IoT48130.2020.9221419.

[28] V. Walter, M. Vrba, and M. Saska, "On training datasets for machine learning-based visual relative localization of micro-scale UAVs," in *2020 IEEE International Conference on Robotics and Automation (ICRA)*, 2020, pp. 10 674–10 680.

[29] P. S. Bithas, E. T. Michailidis, N. Nomikos, D. Vouyioukas, and A. G. Kanatas, "A survey on machine-learning techniques for uav-based communications," *Sensors (Basel)*, vol. 19, no. 23, p. 5170, Nov. 2019. DOI: 10.3390/s19235170.

[30] N. Saeed, S. Guo, K.-H. Park, T. Y. Al-Naffouri, and M.-S. Alouini, "Optical camera communications: Survey, use cases, challenges, and future trends," *Physical Communication*, vol. 37, p. 100 900, 2019.

[31] V. Walter, N. Staub, A. Franchi, and M. Saska, "Uvdar system for visual relative localization with application to leader–follower formations of multirotor uavs," *IEEE Robotics and Automation Letters*, vol. 4, no. 3, pp. 2637–2644, 2019, ISSN: 2377-3766. DOI: 10.1109/LRA.2019.2901683.

[32] J. Zhang, Y. Ding, H. Xu, and Y. Yuan, "An optical flow based moving objects detection algorithm for the uav," in *2019 IEEE 4th International Conference on Computer and Communication Systems (ICCCS)*, 2019, pp. 233–238. DOI: 10.1109/CCOMS.2019.8821661.

[33] C.-W. Chow, Y.-C. Liu, R.-J. Shiu, and C.-H. Yeh, "Adaptive thresholding scheme for demodulation of rolling-shutter images obtained in cmos image sensor based visible light communications," *IEEE Photonics Journal*, vol. 10, no. 6, pp. 1–6, 2018. DOI: 10.1109/JPHOT.2018.2876798.

[34] M. Z. Chowdhury, M. T. Hossan, M. K. Hasan, and Y. Jang, "Integrated rf/optical wireless networks for improving qos in indoor and transportation applications," *Wireless Personal Communications*, vol. 107, pp. 1401 –1430, 2018. DOI: 10.1007/s11277-018-5971-3.

[35] M. K. Hasan, M. Z. Chowdhury, M. Shahjalal, V. T. Nguyen, and Y. Jang, "Performance analysis and improvement of optical camera communication," *Applied Sciences*, 2018. DOI: 10.3390/APP8122527.

[36] N. B. Hassan, Y. Huang, Z. Shou, *et al.*, "Impact of camera lens aperture and the light source size on optical camera communications," *2018 11th International Symposium on Communication Systems, Networks Digital Signal Processing (CSNDSP)*, pp. 1–5, 2018. DOI: 10.1109/CSNDSP.2018.8471766.

[37] V. Walter, N.Staub, M. Saska, and A. Franchi, "Mutual localization of uavs based on blinking ultraviolet markers and 3d time-position hough transform," in *14th IEEE International Conference on Automation Science and Engineering (CASE 2018)*, 2018.

[38] V. Walter, M. Saska, and A. Franchi, "Fast mutual relative localization of uavs using ultraviolet led markers," in *2018 International Conference on Unmanned Aircraft System (ICUAS 2018)*, 2018.

[39] N. T. Le, M. A. Hossain, and Y. M. Jang, "A survey of design and implementation for optical camera communication," *Signal Processing: Image Communication*, vol. 53, 2017.

[40] T.-C. Bui and S. Kiravittaya, "Demonstration of using camera communication based infrared led for uplink in indoor visible light communication," in *2016 IEEE Sixth International Conference on Communications and Electronics (ICCE)*, Ha-Long, Vietnam, 2016, pp. 71–76. DOI: 10.1109/CCE.2016.7562615.

[41] Y. Goto *et al.*, "A new automotive vlc system using optical communication image sensor," *IEEE Photonics Journal*, vol. 8, no. 3, pp. 1–17, Jun. 2016. DOI: 10.1109/JPHOT.2016.2555582.

[42] J. Li, D. H. Ye, T. Chung, M. Kolsch, J. Wachs, and C. Bouman, "Multi-target detection and tracking from a single camera in unmanned aerial vehicles (uavs)," in *2016 IEEE/RSJ International Conference on Intelligent Robots and Systems (IROS)*, 2016, pp. 4992–4997. DOI: 10.1109/IROS.2016.7759733.

[43] P. Luo *et al.*, "Experimental demonstration of rgb led-based optical camera communications," *IEEE Photonics Journal*, vol. 7, no. 5, pp. 1–12, Oct. 2015. DOI: 10.1109/JPHOT.2015.2486680.

[44] A. Ashok, S. Jain, M. Gruteser, N. Mandayam, W. Yuan, and K. Dana, "Capacity of pervasive camera based communication under perspective distortions," in *2014 IEEE International Conference on Pervasive Computing and Communications (PerCom)*, 2014, pp. 112–120. DOI: 10.1109/PerCom.2014.6813951.

[45] G. P. Nava, Y. Kamamoto, T. G. Sato, Y. Shiraki, N. Harada, and T. Moriya, "Image processing techniques for high speed camera-based free-field optical communication," *2013 IEEE International Conference on Signal and Image Processing Applications*, pp. 384–389, 2013. DOI: 10.1109/ICSIPA.2013.6708038.

[46] I. Takai, S. Ito, K. Yasutomi, K. Kagawa, M. Andoh, and S. Kawahito, "Led and cmos image sensor based optical wireless communication system for automotive applications," *IEEE Photonics Journal*, vol. 5, no. 5, pp. 6 801 418–6 801 418, Oct. 2013. DOI: 10.1109/JPHOT.2013.2277881.

[47] N. M. Kwok, H. Y. Shi, G. Fang, and Q. P. Ha, "Intensity-based gain adaptive unsharp masking for image contrast enhancement," in *2012 5th International Congress on Image and Signal Processing*, 2012, pp. 529–533. DOI: 10.1109/CISP.2012.6469772.

[48] N. Otsu, "A threshold selection method from gray-level histograms," *IEEE Transactions on Systems, Man, and Cybernetics*, vol. 9, no. 1, pp. 62–66, 1979. DOI: 10.1109/TSMC.1979.4310076.

[49] S. Kullback and R. A. Leibler, "On information and sufficiency," *The Annals of Mathematical Statistics*, vol. 22, no. 1, pp. 79–86, 1951, ISSN: 00034851. [Online]. Available: http://www.jstor.org/stable/2236703 (visited on 05/23/2024).

A Statistics results of desert experiments

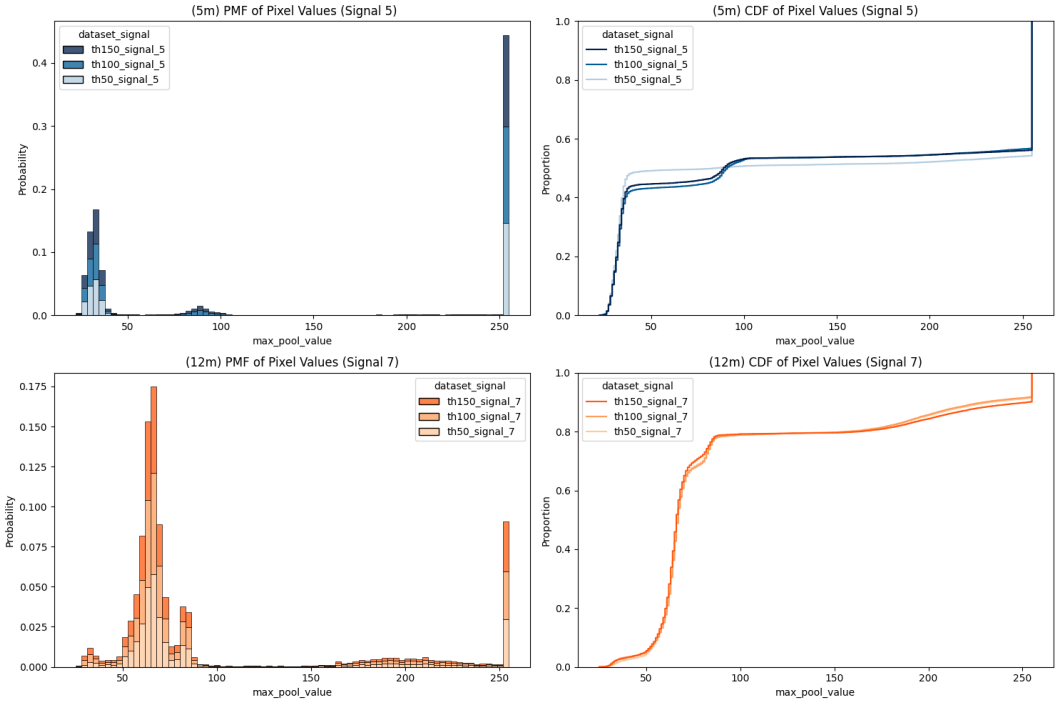

Figure A.1: PMF and CDF from TX (Signal 5) at 5m and TX (Signal 7) at 12m

Table A.1: Statistical comparison between Signal 5 (5 meters) and Signal 7 (10 meters)

Statistic	Signal 5 ON	Signal 5 OFF	Signal 7 ON	Signal 7 OFF
Count	1,631,885.000	1,676,708.000	1,657,246.000	1,314,125.000
Mean	239.791	31.644	131.938	61.255
Std Dev	46.882	9.280	78.428	17.844
Min	50.000	22.000	50.000	22.000
25%	255.000	25.000	68.000	58.000
50%	255.000	32.000	74.000	67.000
75%	255.000	34.000	214.000	70.000
Max	255.000	100.000	255.000	100.000

Table A.2: Statistical comparison between Signal 5 (5 meters) and Signal 7 (12 meters)

Statistic	Signal 5 ON	Signal 5 OFF	Signal 7 ON	Signal 7 OFF
Count	2,677,259.000	2,518,899.000	3,270,466.000	2,533,910.000
Mean	238.473	35.226	124.485	63.509
Std Dev	47.432	13.415	78.638	12.019
Min	50.000	22.000	50.000	25.000
25%	255.000	30.000	64.000	60.000
50%	255.000	32.000	71.000	64.000
75%	255.000	34.000	204.000	68.000
Max	255.000	100.000	255.000	100.000

Table A.3: Statistical comparison between Signal 5 (5 meters) and Signal 7 (15 meters)

Statistic	Signal 5 ON	Signal 5 OFF	Signal 7 ON	Signal 7 OFF
Count	2,553,502.000	2,517,564.000	3,502,441.000	2,740,004.000
Mean	247.721	31.394	117.180	67.051
Std Dev	29.294	5.432	64.212	14.327
Min	50.000	22.000	50.000	24.000
25%	255.000	29.000	68.000	64.000
50%	255.000	31.000	78.000	69.000
75%	255.000	33.000	165.000	73.000
Max	255.000	100.000	255.000	100.000

Table A.4: Statistical comparison between Signal 5 (5 meters) and Signal 7 (20 meters)

Statistic	Signal 5 ON	Signal 5 OFF	Signal 7 ON	Signal 7 OFF
Count	1,926,968.000	1,534,208.000	394,754.000	439,891.000
Mean	202.065	37.691	99.949	50.724
Std Dev	84.417	11.929	44.619	19.155
Min	50.000	23.000	50.000	22.000
25%	133.000	29.000	64.000	30.000
50%	255.000	31.000	76.000	58.000
75%	255.000	50.000	130.000	65.000
Max	255.000	100.000	255.000	100.000

Table A.5: Statistical comparison between Signal 5 (5 meters) and Signal 7 (23 meters)

Statistic	Signal 5 ON	Signal 5 OFF	Signal 7 ON	Signal 7 OFF
Count	7,426,407.000	4,267,125.000	56,982.000	155,917.000
Mean	162.555	52.546	84.249	42.280
Std Dev	93.643	14.570	13.213	21.540
Min	50.000	23.000	50.000	26.000
25%	63.000	35.000	75.000	30.000
50%	207.000	58.000	84.000	31.000
75%	255.000	64.000	94.000	40.000
Max	255.000	100.000	118.000	100.000

Table A.6: Descriptive Statistics for th150 (10m)

Statistic	Signal 5 ON	Signal 5 OFF	Signal 7 ON	Signal 7 OFF
Count	504,266.000	512,974.000	500,376.000	392,448.000
Mean	249.937	31.226	131.183	61.874
Std Dev	26.567	7.328	81.271	15.135
Min	50.000	22.000	50.000	22.000
25%	255.000	26.000	67.000	62.000
50%	255.000	32.000	71.000	67.000
75%	255.000	34.000	227.000	70.000
Max	255.000	100.000	255.000	100.000

Table A.7: Descriptive Statistics for th100 (10m)

Statistic	Signal 5 ON	Signal 5 OFF	Signal 7 ON	Signal 7 OFF
Count	516,135.000	517,323.000	571,537.000	455,982.000
Mean	247.948	30.946	133.429	60.745
Std Dev	29.930	6.851	78.340	18.715
Min	50.000	22.000	50.000	22.000
25%	255.000	25.000	68.000	53.000
50%	255.000	32.000	84.000	66.000
75%	255.000	34.000	216.000	70.000
Max	255.000	100.000	255.000	100.000

Table A.8: Descriptive Statistics for th50 (10m)

Statistic	Signal 5 ON	Signal 5 OFF	Signal 7 ON	Signal 7 OFF
Count	611,484.000	646,411.000	585,333.000	465,695.000
Mean	224.538	32.534	131.128	61.233
Std Dev	64.450	11.911	75.978	19.025
Min	50.000	22.000	50.000	22.000
25%	255.000	25.000	68.000	55.000
50%	255.000	31.000	86.000	67.000
75%	255.000	34.000	204.000	70.000
Max	255.000	100.000	255.000	100.000

Table A.9: Descriptive Statistics for th150 (12m)

Statistic	Signal 5 ON	Signal 5 OFF	Signal 7 ON	Signal 7 OFF
Count	883,575.000	834,497.000	1,004,762.000	793,472.000
Mean	236.293	36.357	125.894	62.867
Std Dev	50.812	15.281	80.635	12.007
Min	50.000	22.000	50.000	25.000
25%	255.000	30.000	64.000	59.000
50%	255.000	32.000	70.000	64.000
75%	255.000	35.000	211.000	68.000
Max	255.000	100.000	255.000	100.000

Table A.10: Descriptive Statistics for th100 (12m)

Statistic	Signal 5 ON	Signal 5 OFF	Signal 7 ON	Signal 7 OFF
Count	957,056.000	867,778.000	1,156,995.000	896,740.000
Mean	233.337	37.035	124.008	63.659
Std Dev	53.842	16.317	77.568	12.443
Min	50.000	23.000	50.000	25.000
25%	255.000	30.000	64.000	60.000
50%	255.000	33.000	71.000	65.000
75%	255.000	35.000	201.000	69.000
Max	255.000	100.000	255.000	100.000

Table A.11: Descriptive Statistics for th50 (12m)

Statistic	Signal 5 ON	Signal 5 OFF	Signal 7 ON	Signal 7 OFF
Count	836,628.000	816,624.000	1,108,709.000	843,698.000
Mean	246.651	32.148	123.705	63.952
Std Dev	32.473	4.391	77.893	11.537
Min	50.000	23.000	50.000	26.000
25%	255.000	30.000	64.000	60.000
50%	255.000	32.000	71.000	65.000
75%	255.000	34.000	202.000	69.000
Max	255.000	100.000	255.000	100.000

Table A.12: Descriptive Statistics for th150 (15m)

Statistic	Signal 5 ON	Signal 5 OFF	Signal 7 ON	Signal 7 OFF
Count	823,173.000	816,698.000	641,858.000	525,615.000
Mean	249.248	31.328	124.381	63.694
Std Dev	25.443	5.042	74.424	13.248
Min	50.000	22.000	50.000	27.000
25%	255.000	29.000	67.000	62.000
50%	255.000	31.000	73.000	67.000
75%	255.000	33.000	196.000	71.000
Max	255.000	100.000	255.000	100.000

Table A.13: Descriptive Statistics for th100 (15m)

Statistic	Signal 5 ON	Signal 5 OFF	Signal 7 ON	Signal 7 OFF
Count	841,872.000	814,615.000	1,350,087.000	1,047,451.000
Mean	248.835	31.462	116.257	67.577
Std Dev	26.240	5.044	62.731	14.565
Min	50.000	23.000	50.000	24.000
25%	255.000	29.000	69.000	64.000
50%	255.000	31.000	79.000	69.000
75%	255.000	34.000	163.000	74.000
Max	255.000	100.000	255.000	100.000

Table A.14: Descriptive Statistics for th50 (15m)

Statistic	Signal 5 ON	Signal 5 OFF	Signal 7 ON	Signal 7 OFF
Count	888,457.000	886,251.000	1,510,496.000	1,166,938.000
Mean	245.250	31.392	114.946	68.092
Std Dev	34.708	6.084	60.514	14.357
Min	50.000	23.000	50.000	24.000
25%	255.000	28.000	69.000	65.000
50%	255.000	31.000	79.000	69.000
75%	255.000	34.000	159.000	75.000
Max	255.000	100.000	255.000	100.000

Table A.15: Descriptive Statistics for th150 (20m)

Statistic	Signal 5 ON	Signal 5 OFF	Signal 7 ON	Signal 7 OFF
Count	622,162.000	499,285.000	20,019.000	24,465.000
Mean	204.848	37.556	134.683	41.582
Std Dev	84.088	12.031	67.832	13.923
Min	50.000	23.000	51.000	23.000
25%	157.000	29.000	60.000	29.000
50%	255.000	31.000	163.000	35.000
75%	255.000	50.000	193.000	57.000
Max	255.000	100.000	255.000	89.000

Table A.16: Descriptive Statistics for th100 (20m)

Statistic	Signal 5 ON	Signal 5 OFF	Signal 7 ON	Signal 7 OFF
Count	647,895.000	512,139.000	62,960.000	81,881.000
Mean	202.596	37.747	123.785	42.301
Std Dev	84.207	12.010	55.868	16.107
Min	50.000	23.000	50.000	23.000
25%	139.000	29.000	64.000	29.000
50%	255.000	31.000	133.000	33.000
75%	255.000	50.000	174.000	60.000
Max	255.000	99.000	237.000	100.000

Table A.17: Descriptive Statistics for th50 (20m)

Statistic	Signal 5 ON	Signal 5 OFF	Signal 7 ON	Signal 7 OFF
Count	656,911.000	522,784.000	311,775.000	333,545.000
Mean	198.906	37.764	92.905	53.462
Std Dev	84.829	11.749	36.786	19.364
Min	50.000	23.000	50.000	22.000
25%	119.000	29.000	64.000	31.000
50%	255.000	31.000	72.000	62.000
75%	255.000	51.000	116.000	66.000
Max	255.000	100.000	237.000	100.000

Table A.18: Descriptive Statistics for th150 (23m)

Statistic	Signal 5 ON	Signal 5 OFF	Signal 7 ON	Signal 7 OFF
Count	2,424,860.000	1,382,999.000	0.000	0.000
Mean	163.824	52.569	NaN	NaN
Std Dev	94.562	14.450	NaN	NaN
Min	50.000	24.000	NaN	NaN
25%	63.000	36.000	NaN	NaN
50%	234.000	58.000	NaN	NaN
75%	255.000	64.000	NaN	NaN
Max	255.000	100.000	NaN	NaN

Table A.19: Descriptive Statistics for th100 (23m)

Statistic	Signal 5 ON	Signal 5 OFF	Signal 7 ON	Signal 7 OFF
Count	2,465,159.000	1,411,193.000	4.000	10.000
Mean	162.584	52.782	105.000	29.400
Std Dev	93.551	14.517	0.000	0.516
Min	50.000	23.000	105.000	29.000
25%	63.000	36.000	105.000	29.000
50%	206.000	59.000	105.000	29.000
75%	255.000	64.000	105.000	30.000
Max	255.000	100.000	105.000	30.000

Table A.20: Descriptive Statistics for th50 (23m)

Statistic	Signal 5 ON	Signal 5 OFF	Signal 7 ON	Signal 7 OFF
Count	2,536,388.000	1,472,933.000	56,978.000	155,907.000
Mean	161.315	52.297	84.248	42.281
Std Dev	92.829	14.727	13.212	21.541
Min	50.000	23.000	50.000	26.000
25%	63.000	35.000	75.000	30.000
50%	185.000	58.000	84.000	31.000
75%	255.000	64.000	94.000	40.000
Max	255.000	100.000	118.000	100.000

B Statistics results of real world experiments

Table B.1: Adaptive Otsu Thresholding (1000 us)

Nearest Distance	Total Entries	Total Errors	Error Rate
5	7,854	564	0.071811
10	6,288	542	0.086196
15	6,424	3,538	0.550747
20	6,348	4,645	0.731727
25	6,492	6,373	0.981670
30	8,657	8,650	0.999191

Table B.2: KL Adaptive Method (1000 us)

Nearest Distance	Total Entries	Total Errors	Error Rate
5	7,842	754	0.096149
10	6,685	1,061	0.158714
15	9,135	5,945	0.650794
20	6,846	6,115	0.893222
25	6,378	6,367	0.998275
30	9,109	9,101	0.999122

Table B.3: Standard Static Thresholding (1000 us)

Nearest Distance	Total Entries	Total Errors	Error Rate
5	7,332	579	0.078969
10	6,282	506	0.080548
15	6,325	3,537	0.559209
20	4,817	4,690	0.973635
25	4,266	4,236	0.992968
30	4,643	4,475	0.963816

Table B.4: Adaptive Otsu Thresholding (500 us)

Nearest Distance	Total Entries	Total Errors	Error Rate
5	6,888	373	0.054152
10	6,261	274	0.043763
15	6,346	1,534	0.241727
20	6,483	5,575	0.859941
25	6,410	6,338	0.988768
30	6,881	6,797	0.987792

Table B.5: KL Adaptive Method (500 us)

Nearest Distance	Total Entries	Total Errors	Error Rate
5	9,596	2,098	0.218633
10	7,451	1,447	0.194202
15	8,109	4,945	0.609816
20	6,767	6,585	0.973105
25	6,204	6,110	0.984848
30	7,374	7,238	0.981557

Table B.6: Standard Static Thresholding (500 us)

Nearest Distance	Total Entries	Total Errors	Error Rate
5	11,648	688	0.059066
10	6,288	263	0.041826
15	6,231	3,714	0.596052
20	4,203	3,826	0.910302
25	2,108	1,464	0.694497
30	2,968	2,944	0.991914

Table B.7: Special Scenario: Experiment at Night using Otsu Adaptive Method

Nearest Distance	Total Entries	Total Errors	Error Rate
5	3,639	407	0.111844
10	8,725	988	0.113238
15	26,407	2,093	0.079259
20	5,250	309	0.058857
25	5,305	411	0.077474
30	38,511	35,394	0.919062

Table B.8: Otsu Method for the Heading Experiment

Nearest Distance	Total Entries	Total Errors	Error Rate
5	16,914	10,882	0.643372
10	6,232	4,285	0.687580
15	6,193	4,251	0.686420
20	5,086	3,067	0.603028
25	4,339	2,440	0.562342
30	4,706	3,610	0.767106

Table B.9: KL Method for the Heading Experiment

Nearest Distance	Total Entries	Total Errors	Error Rate
5	9,625	5,467	0.568000
10	6,240	4,286	0.686859
15	6,148	4,223	0.686890
20	5,201	3,397	0.653144
25	4,499	3,927	0.872861
30	4,837	4,725	0.976845

Table B.10: Static Method for the Heading Experiment

Nearest Distance	Total Entries	Total Errors	Error Rate
5	6,026	837	0.138898
10	4,194	2,259	0.538627
15	4,192	2,162	0.515744
20	4,197	2,369	0.564451
25	4,353	3,895	0.894785
30	3,304	3,156	0.955206

C Source code for Adaptive Algorithm

Github Repository

https://github.com/MarlonRiv/uvdar_core

https://github.com/MarlonRiv/uvdar_core/blob/master/src/detector.cpp

https://github.com/MarlonRiv/uvdar_core/blob/master/include/detect/uv_led_detect_adaptive.cpp

https://github.com/MarlonRiv/uvdar_core/blob/master/include/detect/uv_led_detect_adaptive.h

D Used Software

In compliance with ethical principles and Methodical guideline No. 5/2023.

I declare that AI tools were not used for the generation of any of the texts in this thesis.

- AI generative tools were only used for proofreading and evaluation of the written texts for improvement and review of clarity.
- During the development of the technical part, Github Copilot was only used for auto-completion used for testing and ChatGPT for learning and as a source for consultation on modern C++ coding practices for optimizing the proposed solution.